Peer-reviewed version available at J. Mar. Sci. Eng. 2018, 6, 53; doi:10.3390/jmse6020053

Article

Marine Turbine Hydrodynamics by a Boundary Element Method with Viscous Flow Correction

Francesco Salvatore*, Zohreh Sarichloo, and Danilo Calcagni

CNR-INSEAN, National Research Council, Marine Technology Research Institute
Via di Vallerano 139, 00128 Rome, Italy
* Correspondence: francesco.salvatore@cnr.it; Tel.: +39-06-5029-9313

Abstract: A computational methodology for the hydrodynamic analysis of horizontal axis marine current turbines is presented. The approach is based on a boundary integral equation method for inviscid flows originally developed for marine propellers and adapted here to describe the flow features that characterize hydrokinetic turbines. To this purpose, semi-analytical trailing wake and viscous-flow correction models are introduced. A validation study is performed by comparing hydrodynamic performance predictions with two experimental test cases and with results from other numerical models in the literature. The capability of the proposed methodology to correctly describe turbine thrust and power over a wide range of operating conditions is discussed. Viscosity effects associated to blade flow separation and stall are taken into account and predicted thrust and power are comparable with results of blade element methods that are largely used in the design of marine current turbines. The accuracy of numerical predictions tend to reduce in cases where turbine blades operate in off-design conditions.

Keywords: Marine Current Turbine, Hydrodynamics, Boundary Element Methods, Trailing wake Models, Viscous Flow Correction

1. Introduction

Marine or hydrokinetic turbines for the production of renewable energy from tidal and ocean currents is a rapidly growing technology. Large scale installations mainly address horizonthal-axis turbines installed on structures fixed to the seabed or supported by floating platforms.

The relatively fast maturation of hydrokinetic turbine technology as compared to other ocean energy harvesting systems is partly due to experience gained over the last decades in the wind energy sector. In most cases the aspect of marine turbine blades resembles wind rotor blades except for the aspect ratio that is quite smaller to resist hydrodynamic loads in water. It is then not surprising that Blade Element Momentum Methods (simply, BEM) originally developed for wind turbines are extensively used for analysis and design of tidal and ocean current turbines, see *e.g.* [1]. BEM provides fast and reliable estimates of turbine performance if suitable tuning is applied to overcome important methodology weaknesses [2], [3]. Specifically, blade loading is derived by prescribed lift and drag properties of two-dimensional profiles and semi-empirical three-dimensional flow corrections are necessary to account for blade tip effects, blade/hub interaction, number of blades.

In contrast to this, the hydrodynamic design of marine propellers is typically based on boundary element or panel methods that, under limiting inviscid-flow assumptions, provide a consistent representation of the three-dimensional flow around rotors in steady or unsteady flow. To avoid confusion with blade element (momentum) methods, the terminology Boundary Integral Equation Method (BIEM) is used here. In spite of that, only few example exist of applications of BIEMs to hydrokinetic turbines, see *e.g.* Young et al. [4], Kinnas et al. [5]. Results in the literature highlight the difficulty of boundary element methods to correctly describe the hydrodynamic performance of turbines designed to extract energy from an onset flow. A major difficulty is that turbine blades frequently operate at high angle of attack and viscosity induced separation and stall significantly affect

generated thrust and power. Baltazar & Falcão de Campos [6], [7] address the problem by comparing different models to correct inviscid-flow predictions by BIEM.

The problem is tackled in the present work by the development of original viscous flow and trailing wake models that are integrated into a BIEM originally developed for marine propellers, see *e.g.* Salvatore et al. [8],[9], [10]. In the proposed methodology, the trailing wake geometry is determined by a semi-analytical model with wake pitch alignment consistent with turbine-induced velocity perturbation and an experimental-based definition of the expansion rate of the streamtube downstream the rotor plane. Inspired to blade element methods, a viscous-flow correction is determined by comparing distributions of blade loads by the inviscid-flow BIEM and lift and drag properties of representative blade sections under flow separation and stall. Lift and drag data are obtained from available experimental data or from numerical predictions by two-dimensional viscous-flow solvers.

The resulting methodology with Viscous-Flow Correction (VFC) is referred to here as BIEM-VFC. A validation study for the proposed computational model is addressed by considering two case studies taken from the literature with experimental results for three-bladed model turbines. Specifically, Gaurier et al. [11] present results from the first round-robin test on tidal turbines carried out in the framework of the EU-FP7 MaRINET Project [12], with turbine performance measurements from two towing tanks (Strathclyde University and CNR-INSEAN) and two flume tanks (IFREMER and CNR-INSEAN). Next, Bahaj et al. [13] present a detailed characterization of marine current turbine performance by considering the effects of blade pitch variations. For this case study, BIEM-VFC is also compared with other numerical models based on BEM and BIEM. Results of the comparative analyis provide a clear overview of the accuracy of the proposed BIEM-VFC methodology and its range of applicability as a marine current turbine analysis and design tool.

The paper is organised as follows. The theoretical and computational BIEM-VFC methodology is outlined in Section 2, with details of viscous flow and trailing wake models. The validation study is addressed in Sections 3 to 5, while strenghts and weaknesses of the methodology are discussed in Section 6.

2. Theoretical model

The computational model proposed here for the hydrodynamic analysis of marine current turbines is based on a Boundary Integral Equation Method (BIEM) that is valid under inviscid flow assumptions. The methodology has been originally developed at CNR-INSEAN to study marine propulsors, see *e.g.*, Salvatore et al. [8], [9], and Pereira et al. [10].

The extension of the methodology to analyse marine turbine flows requires the introduction of suitable models to describe trailing vorticity dynamics and to correct blade loads when turbine blades undergo flow separation and stall. In this section, the original BIEM is briefly reviewed and models specifically developed for turbine trailing vorticity and viscosity effects are described in details.

Assuming the onset flow is incompressible and inviscid, the perturbation velocity $\mathbf{v}$ induced by the turbine may be described by a scalar potential as $\mathbf{v} = \nabla\varphi$, and general mass and momentum equations are dramatically simplified. Mass conservation yields the Laplace equation for the perturbation velocity potential, $\nabla^2\varphi = 0$, while the momentum equation reduces to the Bernoulli Equation for pressure p

$$\frac{\partial\varphi}{\partial t} + \frac{1}{2}\|\nabla\varphi + \mathbf{v}_I\|^2 + \frac{p}{\rho} + gz_0 = \frac{1}{2}\|\mathbf{v}_I\|^2 + \frac{p_0}{\rho}, \tag{1}$$

where p_0 is the free-stream reference pressure, and $\mathbf{v}_I = \mathbf{w} + \boldsymbol{\Omega} \times \mathbf{x}$ is the inflow velocity as seen from an observer fixed with blades rotating at angular velocity $\boldsymbol{\Omega}$ while $\mathbf{w}$ is the onset flow velocity. In case of uniform inflow aligned to turbine axis x, one has $\boldsymbol{\Omega} = \Omega\mathbf{e}_x$, $\mathbf{w} = V\mathbf{e}_x$ with $\mathbf{e}_x$ unit vector along x, see Fig. 1. Finally, gz_0 is the hydrostatic head term referred to a reference vertical position $z = 0$.

The Laplace equation for φ is solved via a boundary integral formulation where problem unknowns are distributed on the body surface and on its *trailing wake*. By potential flow theory for lifting bodies, the trailing wake denotes a zero-thickness layer where vorticity generated by lifting

Preprints (www.preprints.org) | NOT PEER-REVIEWED | Posted: 4 April 2018 doi:10.20944/preprints201804.0048.v1

Peer-reviewed version available at J. Mar. Sci. Eng. 2018, 6, 53; doi:10.3390/jmse6020053

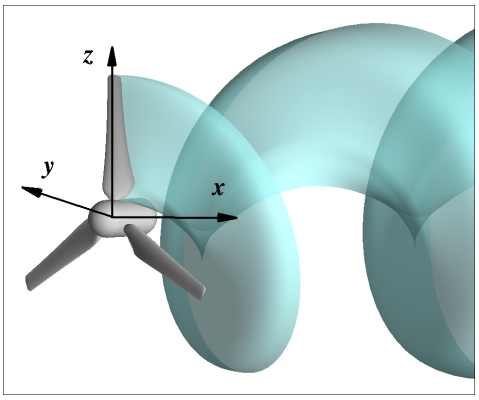

Figure 1. Sketch of the frame of reference associated to the solid boundary describing an isolated turbine and the surface of trailing wake shed by one blade.

surfaces is shed into the downstream flow. Through a classical derivation (see, *e.g.*, Morino [14]) the following boundary integral representation for φ at an arbitrary field point $\mathbf{x}$ is obtained

$$E(\mathbf{x})\,\varphi(\mathbf{x}) \;=\; \oint_{\mathcal{S}_{B\cup N}} \left(\frac{\partial \varphi}{\partial n} G - \varphi \frac{\partial G}{\partial n}\right) d\mathcal{S}(\mathbf{y}) \;-\; \int_{\mathcal{S}_W} \Delta\varphi \frac{\partial G}{\partial n} d\mathcal{S}(\mathbf{y}). \tag{2}$$

Dealing with isolated turbines modelling by BIEM, a typical schematization is to represent the device as an assembly of blades attached to a nacelle of finite length immersed in an unbounded flow, as sketched in Fig.1. In the above equation, $\mathcal{S}_{B\cup N}$ denotes the solid surface combining blades $\mathcal{S}_B$ and nacelle $\mathcal{S}_N$, while $\mathcal{S}_W$ is the trailing wake. Quantity $\mathbf{n}$ is the unit normal to these surfaces, pointing outward on solid boundaries and from pressure to suction sides at blade trailing edges to define the orientation on the wake. The symbol Δ in Eq. (2) is used to denote discontinuity of velocity potential across the trailing wake surface defined according to the convention used for the unit normal to $\mathcal{S}_W$, whereas $E(\mathbf{x})$ is a function that makes the same equation to be valid for points $\mathbf{x}$ on the body surface ($E = 1/2$) or inside the fluid domain, $E = 1$. Moreover, quantities $G, \partial G/\partial n$ are unit source and dipoles in the unbounded three-dimensional space and depend only from the mutual position between the collocation point $\mathbf{x}$ and the influencing point $\mathbf{y}$ on the boundary surfaces. A distinguishing feature of the present formulation is that analytical expressions are used to evaluate the exact contributions of source and dipole terms on hyperboloidal quadrilateral surface elements, see [14] for details.

Boundary conditions for the velocity potential are imposed at infinity (vanishing perturbation φ), on solid surfaces (impermeability, $\partial\varphi/\partial n = -\mathbf{v}_I \cdot \mathbf{n}$) and on the trailing wake, where convection of vorticity generated on blades is imposed and a Kutta-Morino condition is used to impose identity between velocity potential difference at blade trailing edge pressure and suction sides and $\Delta\varphi$ on the wake.

Equation (2) with $E = 1/2$ and related boundary conditions represents a boundary integral equation whose solution determines φ on the body surface. By discretizing boundaries $\mathcal{S}_{B\cup N}$ and $\mathcal{S}_W$ into surface panels, and enforcing Eq. (2) at centroids of body panels, a linear set of algebraic equations is obtained. The wake surface $\mathcal{S}_W$ can be determined as a part of the solution by a wake-alignment iterative procedure, as described in [15]. A faster and more robust approach is used in the present study as described in Sect. 2 below.

Once Eq. (2) is numerically solved, the velocity potential and its gradient are known on the body surface and pressure can be evaluated using the Bernoulli Eq. (1). Hydrodynamic loads generated by the turbine are then obtained by integrating pressure and tangential stress τ over the blades surface. In

particular, the force contribution by a blade element of radial extension dr and chord c can be written as

$$\mathrm{d}\mathbf{f}(r) \;=\; \mathrm{d}\mathbf{f}_p(r) + \mathrm{d}\mathbf{f}_\tau(r) \;=\; (-p\,\mathbf{n} + \tau\,\mathbf{t})\; d\mathcal{S}, \tag{3}$$

where $d\mathcal{S} \;=\; c\,\mathrm{d}r$, $\mathbf{t}$ is the unit vector tangent to the surface and aligned to the local flow and quantities $\mathbf{f}_p, \mathbf{f}_\tau$ denote, respectively, contributions by normal (pressure) and tangential (friction) stress. Integrating elementary forces on all blades, turbine thrust T and torque Q follow

$$T = \int_{S_B} \mathbf{f}\cdot\mathbf{e}_x\, d\mathcal{S}, \qquad Q = \int_{S_B} (\mathbf{x}\times\mathbf{f})\cdot\mathbf{e}_x\, d\mathcal{S}. \tag{4}$$

Surface stress τ is not part of the inviscid-flow solution and could be evaluated by a coupled viscous/inviscid model in which BIEM is combined with a boundary-layer model, as described in Salvatore et al. [8]. A simplified approach popular in marine propeller models consists in estimating quantity τ from formulas valid for attached laminar and turbulent flow over a flat plate, see *e.g.* [16]

$$\begin{aligned} C_F \;&=\; 1.328/\sqrt{Re_r} \qquad (Re_r < 10^5) \\ C_F \;&=\; 0.075/\left(log_{10}(Re_r) - 2\right)^2 \quad (Re_r \geq 10^5) \end{aligned} \tag{5}$$

where $C_F = \tau/\frac{1}{2}\rho V_I^2(r)$ is the friction coefficient, and

$$Re_r \;=\; c(r)V_I(r)/\nu \;=\; c(r)\sqrt{V^2 + (\Omega r)^2}/\nu, \tag{6}$$

defines the Reynolds number characterizing the flow around the blade section at radius r, where ν is the water kinematic viscosity.

The accuracy of this approximated viscosity correction to hydrodynamic loads by BIEM is typically limited to attached flows on blade sections at low angle of attack. The VFC approach proposed here aims to cope with a wider range of conditions including flow separation and stall, as outlined in Section 2.2.

2.1. Trailing wake model

In the present study, a semi-analytical model is used to determine the wake surface $\mathcal{S}_W$ in Eq. (2). The wake is defined as a generalised helicoidal surface with distributions of axial pitch and radial expansion of the streamtube downstream the rotor that are consistent with the operating mode of hydrokinetic turbines.

For the axial pitch, two regions are considered: the *tip-vortex* region and the *blade wake* extending spanwise between vortices released at blade root and tip. In the blade wake, trailing vortices are convected downstream with velocity given as the average of the onset flow speed and of the velocity perturbation induced by the wake itself, $\mathbf{v}_w$. A boundary integral representation of $\mathbf{v}_w$ is obtained by taking the gradient of the velocity potential equation (2). Here, an approximated representation of this velocity field across the fluid region of interest is obtained by using BIEM to evaluate $\mathbf{v}_w$ at the rotor plane and imposing a linear variation downstream to match a given farfield distribution.

Then, the axial component of the wake-induced velocity, $v_{x,w} = \mathbf{v}_w\cdot\mathbf{e}_x$, may be written as

$$v_{x,w} \;=\; (1-\xi_x)\,\frac{\partial\tilde{\varphi}}{\partial x}\Big|_{RP} \;+\; \xi_x\, v_{x,w}\big|_{FF}, \tag{7}$$

where ξ_x is a normalised abscissa with $\xi_x = 0$ at rotor trailing edge and $\xi_x = 1$ at the downstream end of the discretised wake surface. Consistent with Betz theory [17], the axial induced velocity at farfield $v_{x,w}|_{FF}$ is twice the intensity at the rotor plane. Symbol $(\tilde{})$ denotes wake-induced velocity potential obtained from the gradient of Eq. (2), while subscript RP refers to the rotor plane axial position.

Preprints (www.preprints.org) | NOT PEER-REVIEWED | Posted: 4 April 2018 doi:10.20944/preprints201804.0048.v1

Peer-reviewed version available at J. Mar. Sci. Eng. 2018, 6, 53; doi:10.3390/jmse6020053

In the tip-vortex region, Okulov & Sørensen [18] describe a trailing vortex shedding model with axial velocity given as the average between velocity in the blade wake, Eq. (7), and the unperturbed axial velocity V outside the streamtube. Thus, denoting by $\phi_{w,0}$ the hydrodynamic pitch associated to the unperturbed flow, one obtains the following expressions for the wake pitch ϕ_w

$$\phi_{w,bla}(x,r) = \left(1+\frac{v_{x,w}(x,r)}{V}\right)\phi_{w,0}; \qquad \phi_{w,tip}(x) = \frac{1}{2}\left(\phi_{w,bla}(x,\hat{r}) + \phi_{w,0}\right), \tag{8}$$

$$\phi_w(x,r) = \xi_r\phi_{w,tip}(x) + (1-\xi_r)\phi_{w,bla}(x,r),$$

where pedices bla and tip denote, respectively, blade wake and tip vortex, and ξ_r is a radial weight function (in the present analysis, $\xi_r = (r/R)^3$ has been used, where R is the turbine radius). In the evaluation of $\phi_{w,tip}$, the blade wake pitch $\phi_{w,bla}$ is evaluated at a representative radial station $\hat{r}$.

Next, the radial expansion of the wake streamtube donwstream the rotor plane is determined as

$$r = R + r_0\left(1-e^{-\xi_x/C_2}\right), \tag{9}$$

where constants r_0, C_2 are derived from experimental data describing the wake evolution of hydrokinetic turbines over a range of operating conditions. In the present study, wake flow measurements by Micek et al. [19] (here referred to as IFREMER rotor) and by Del Frate et al. [20] (SABELLA rotor) have been considered, see Fig. 2. The assumption is that at short distance from the rotor, trailing wake expansion is weakly dependent by the rotor shape and a general trend can be derived from flow measurements.

Combining Eqs. (7) to (9), the generalised helicoidal surface defining the trailing wake $\mathcal{S}_W$ is obtained. In fact, the evaluation of the velocity potential $\tilde{\varphi}$ in Eq. (7) depends on the definition of surface $\mathcal{S}_W$ in Eq. (2) and hence an iterative procedure is required. In the numerical analysis addressed in the present work, it has been found that the iteration converges after few steps.

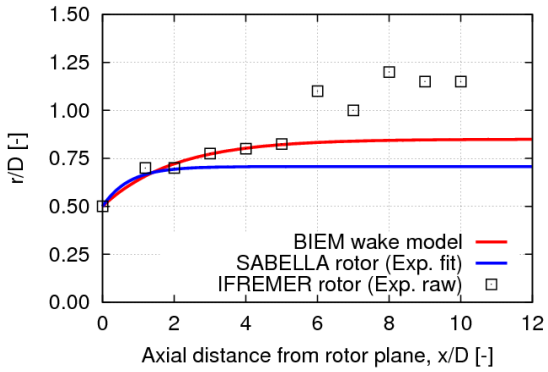

Figure 2. Streamtube radius downstream rotor plane from Eq. (9) and comparative data from experiments.

2.2. Viscous-flow correction model

Assumptions of inviscid, irrotational flow underlying BIEM yield that turbine hydrodynamics is studied by fast numerical solutions of a linear problem with unknowns distributed only on the solid surface of the turbine. Unfortunately, turbine performance is dramatically affected by blade flow separation and stall and hence neglecting viscosity effects may result into completely unreliable predictions of turbine hydrodynamic loads and power output.

A methodology is proposed here to correct blade loads predicted under inviscid-flow assumptions by a procedure that preserves the reduced computing effort typical of BIEM. The idea is to *(i)* identify conditions where blade flow is subject to boundary layer separation and stall and *(ii)* estimate the

Preprints (www.preprints.org) | NOT PEER-REVIEWED | Posted: 4 April 2018 doi:10.20944/preprints201804.0048.v1

Peer-reviewed version available at J. Mar. Sci. Eng. 2018, 6, 53; doi:10.3390/jmse6020053

effect of viscosity on blade loads under such conditions. The BIEM model including this viscous-flow correction is hereafter referred to as BIEM-VFC.

To this purpose, sectional loads along blade span evaluated by BIEM are compared to lift and drag properties of two-dimensional (2D) profiles describing blade sections. Equivalence between operating conditions of three-dimensional rotating blade sections and corresponding 2D profiles is enforced in terms of local Reynolds number Re_r (see Section above) and of the *effective* angle of attack α_e.

Quantity α_e defines the angle of attack where wake-induced velocity contributions are accounted for to evaluate the total velocity incoming to blade sections. A graphical definition of α_e is given in Fig. 3, where inflow velocity components and hydrodynamic force components for a turbine blade section at radius r are sketched. Axial and tangential induced velocity components, respectively Δu_i and Δv_i, represent three-dimensional flow effects induced by trailing vortices shed by blades. These quantitites are zero in case of 2D flow around a lifting surface of infinite span and the effective and nominal angle of attack α coincide.

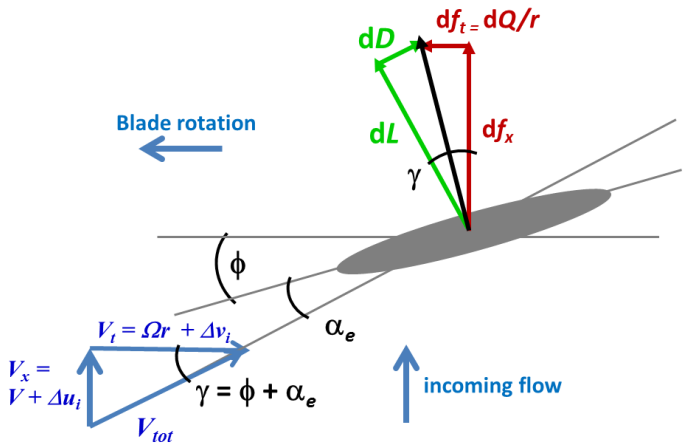

Figure 3. Inflow velocity components and hydrodynamic force components on turbine blade section at radius r.

Lift and drag properties representative of blade section shape and operating conditions (α_e, Re_r) are deduced from 2D foil polar curves, as sketched in Fig. 4. Flow separation occurs when the lift curve departs from linear dependence with incidence α (points labelled as SE+, SE-), while stall occurs when lift drops as α increases in absolute value and drag has an abrupt rise (point ST).

Inviscid-flow solutions by BIEM determine blade sectional loads that are consistent with linear relationship between lift and angle of attack and, using the flat-plate analogy in Eq. (5) with minimum drag reflecting attached flow conditions (curves in red in Fig. 4). The comparison between sectional lift and drag properties motivates the following definition of factors to correct sectional loads by BIEM to represent both attached and separated flow conditions:

$$\begin{aligned} \mathcal{K}_D(\alpha_e, Re_r) &= \mathrm{d}D_{2D}/\mathrm{d}D_{2D}^{inv} \\ \mathcal{K}_L(\alpha_e, Re_r) &= \mathrm{d}L_{2D}/\mathrm{d}L_{2D}^{inv} \end{aligned} \tag{10}$$

where D_{2D}^{inv} and L_{2D}^{inv} are, respectively, drag and lift per unit length determined under inviscid 2D flow conditions (*i.e.* by a 2D BIEM) at angle of attack α_e, while D_{2D} and L_{2D} are profile drag and lift under 2D viscous flow conditions.

Once quantities $\mathcal{K}_D, \mathcal{K}_L$ are known, blade loads correction is obtained through the following procedure. From the BIEM solution, sectional contributions to axial force $\mathrm{d}f_x$ and tangential force $\mathrm{d}f_t$

Preprints (www.preprints.org) | NOT PEER-REVIEWED | Posted: 4 April 2018 doi:10.20944/preprints201804.0048.v1

Peer-reviewed version available at J. Mar. Sci. Eng. 2018, 6, 53; doi:10.3390/jmse6020053

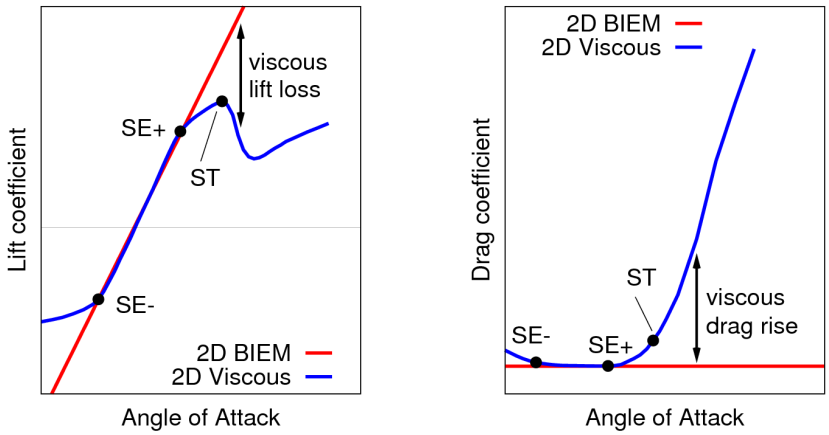

Figure 4. Lift and drag curves of two-dimensional profile: viscous-flow compared with corresponding quasi-inviscid flow.

are determined from Eq. (3). Next, wake-induced velocity along blade span is determined by taking the gradient of Eq. (2) (with $E = 1$), and the radial distribution of the effective angle of attack $\alpha_e(r)$ is evaluated. Radial distributions of sectional drag and lift $\mathrm{d}D, \mathrm{d}L$ follow by projecting force in direction normal and tangent to the effective inflow, as sketched in Fig. 3, where ϕ is the angular pitch of blade section at radius r.

Separating pressure-induced and friction-induced contributions to force $\mathrm{d}\mathbf{f}$ as defined in Eq. (3), lift and drag contributions are also splitted into pressure-induced and friction-induced terms. Correction factors from Eq. (10), yield

$$\begin{aligned} \mathrm{d}\hat{L}_p &= \mathcal{K}_L \mathrm{d}L_p, \qquad & \mathrm{d}\hat{D}_p &= \mathcal{K}_L^2 \mathrm{d}D_p \\ \mathrm{d}\hat{L}_\tau &= \mathcal{K}_D \mathrm{d}L_\tau, \qquad & \mathrm{d}\hat{D}_\tau &= \mathcal{K}_D \mathrm{d}D_\tau \end{aligned} \tag{11}$$

where symbol $(\hat{})$ labels viscous-flow corrected quantities. While corrections for pressure-induced lift L_p and friction-induced drag D_τ are obvious, the assumption made here is that correction factor for drag $\mathcal{K}_D$ can be used to account for flow separation and stall effects on friction-induced lift L_τ. Pressure-induced drag D_p correction by $\mathcal{K}_L^2$ stems from the approximated relationship between induced drag and lift that is broadly valid for lifting surfaces. Numerical studies prove that contributions from *diagonal* terms L_τ and D_p are very small as compared to, respectively, contributions D_τ, L_p.

Converting lift and drag back to respectively axial and tangential load components yields quantitity $\mathrm{d}\hat{f}_x$ that integrated along blade span returns corrected blade axial force, while quantity $\mathrm{d}\hat{Q} = \mathrm{d}\hat{f}_t r$ returns corrected blade torque. Summing on all blades, turbine corrected thrust $\hat{T}$ and torque $\hat{Q}$ are obtained (formally, Eq. (4) with $\mathbf{f}$ replaced by $\hat{\mathbf{f}}$).

A full exploitation of the viscosity correction model described above implies that an iterative procedure is enforced to make the potential flow solution consistent with the modified loading on blades. No iteration has been considered in the present analysis and the subject is briefly address later in Section 6.

3. Case studies for validation of computational model

Numerical applications of the proposed computational model are discussed by considering two case studies taken from the literature. Both cases address three-bladed model turbines designed for research activity.

For a turbine having radius R, swept area $A = \pi R^2$, rotating at angular speed $\Omega = 2\pi n$ in a current with nominal freestream velocity V, the Tip Speed Ratio (TSR or λ) is defined as

$$\lambda = \Omega R / V.$$

Turbine performance is described through thrust, torque and power coefficients, respectively C_T, C_Q, C_P, defined as

$$C_T = \frac{T}{\frac{1}{2}\rho A V^2}, \qquad C_Q = \frac{Q}{\frac{1}{2}\rho A V^2 R}, \qquad C_P = \frac{\Omega Q}{\frac{1}{2}\rho A V^3} = C_Q \cdot \mathrm{TSR}$$

and $P = \Omega Q$ is the power generated by the turbine.

3.1. Fixed pitch turbine

Gaurier et al. [11] describe a 700 mm diameter, fixed-pitch model turbine developed at IFREMER, France. The model has been the subject of the first round-robin test on tidal turbines carried out in the framework of the EU-FP7 MaRINET Project [12], with turbine performance measurements from two towing tanks (Strathclyde University and CNR-INSEAN) and two flume tanks (IFREMER and CNR-INSEAN). Turbine performance curves measured at inflow speed between 0.6 and 1.2 m/s. are presented as mean values and standard deviations.

Main turbine geometry parameters are summarized in Table 1. A full description is given in [11]. This testcase is referred to here as the IFREMER-FP turbine.

Table 1. IFREMER-FP turbine main geometry parameters.

Rotor diameter, D	700 [mm]
Blades number, Z	3
Pitch angle at 70% span, Φ	7.3 [deg]
Thickness ratio, 75% span, t/c	0.21
Hub/rotor diameter ratio	0.131
Blade section profile	NACA 63-4xx

3.2. Variable pitch turbine

Bahaj et al. [13] consider a 800 mm diameter, variable-pitch model turbine developed at the University of Southampton (U.K.). This model was analysed by extensive towing tank and cavitation tunnel tests. Experimental data provide turbine performance at different blade pitch settings, with blades rotated about the spanwise axis over a range of 15 degrees, from $\Phi = 15°$ to $30°$, while $\Phi = 20°$ is taken as the design condition. This pitch definition refers to the nose-tail angle of the blade at radius $r/R = 0.2$. Turbine performance curves are available for inflow speed between 0.8 and 2.0 m/s (cavitation tunnel tests) and between 0.8 and 1.5 m/s (towing tank tests).

Main turbine geometry parameters are summarized in Table 2, while a complete description can be found in [13]. This testcase is referred to here as the UoS-VP turbine.

Table 2. UoS-VP turbine geometry parameters.

Rotor diameter, D	800 [mm]
Blades number, Z	3
Pitch angle at 20% span, Φ	15, 20, 25, 27, 30 [deg]
Thickn. ratio, 75% span, t/c	0.151
Hub/rotor diameter ratio	0.125
Blade section profile	NACA 63-8xx

Preprints (www.preprints.org) | NOT PEER-REVIEWED | Posted: 4 April 2018 doi:10.20944/preprints201804.0048.v1

Peer-reviewed version available at J. Mar. Sci. Eng. 2018, 6, 53; doi:10.3390/jmse6020053

4. Fixed pitch turbine study

The analysis of the IFREMER-FP turbine performance is performed by considering experimental conditions corresponding to the highest inflow speed, $V = 1.2$ m/s. This choice is motivated to avoid a too small Reynolds number characterizing the blade flow. The Tip Speed Ratio λ is varied between zero and 8. Comparing with the physical model in [11], it may be noted that the stanchion supporting the turbine is not described in numerical simulations. Similarly, the nacelle portion downstream the turbine hub is not present in the computational model.

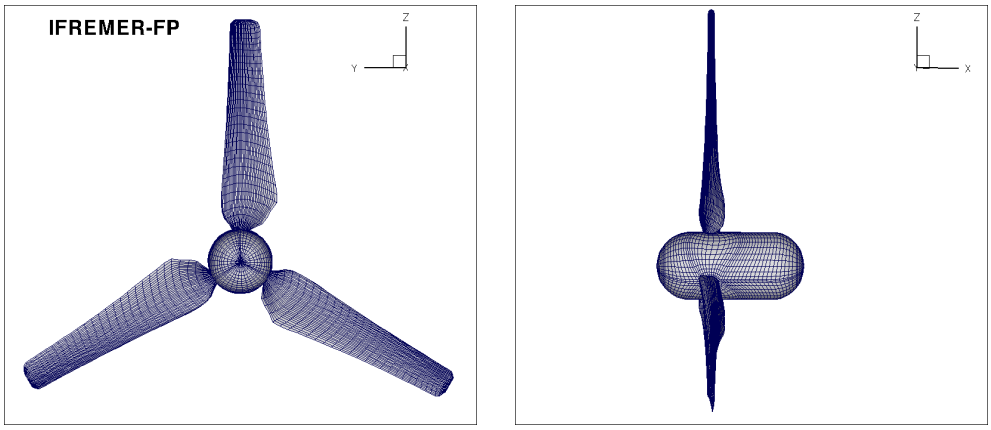

Figure 5. IFREMER-FP turbine. Computational grid used for calculations by BIEM.

Blade and hub surface discretization parameters are determined as the result of a grid sensitivity study. Each blade is discretized into M_B elements chordwise from leading edge to trailing edge and N_B elements spanwise. Four blade grid levels with $M_B = 24, 36, 48, 60$ and $N_B = 20, 30, 40, 50$ are considered. Hub and wake surface discretizations are built according to blade grid refinement level. Figure 6 presents inviscid-flow thrust and torque predicted by BIEM using the four grids. Three representative TSR values are considered. The torque coefficent evaluated by including the viscous-flow correction is also presented to highlight that the VFC model has no effect on the sensitivity of results to grid refinement. From these results it is concluded that a discretization with $M_B = 36, N_B = 30$ is adequate to minimise the effect of further grid refinement on results. In this case, the hub surface is divided into 42 and 54 elements, respectively, in circumferential and longitudinal directions, and the wake is discretized into 36 elements along radius and 60 elements streamwise per revolution. The wake portion considered in the numerical solution of Eq. (2) extends for 10 revolutions.

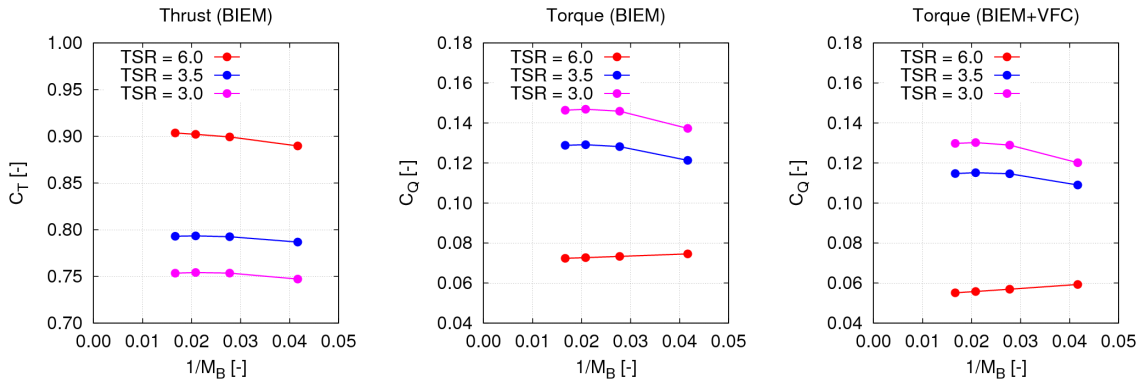

Figure 6. IFREMER-FP turbine. Grid sensitivity study.

Preprints (www.preprints.org) | NOT PEER-REVIEWED | Posted: 4 April 2018 doi:10.20944/preprints201804.0048.v1

Peer-reviewed version available at J. Mar. Sci. Eng. 2018, 6, 53; doi:10.3390/jmse6020053

The trailing wake model described in Section 2 is used to determine the turbine wake surface. Figure 7 maps the intensity of wake-induced velocity evaluated by BIEM at axial locations corresponding to rotor blade trailing edge and at different radial positions over a range of operating conditions identified by the parameter *TSR* . The resulting surfaces for three representative values of

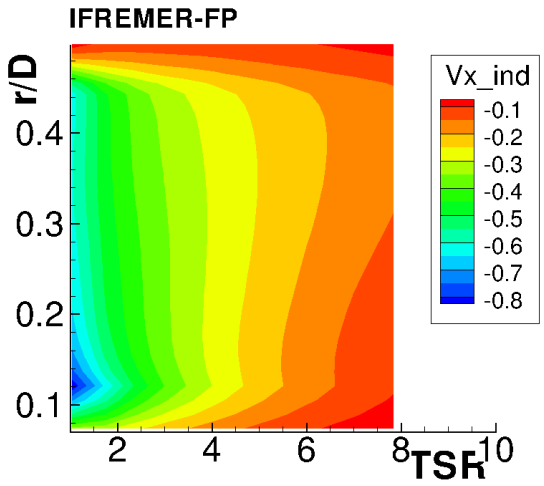

Figure 7. IFREMER-FP turbine. Calculated axial induced velocity distribution at rotor plane.

TSR are shown in Fig. 8. The effect of *TSR* on wake axial pitch is clear: trailing vortices are rapidly shed away from the rotor at low *TSR* , while wake spirals pack-up close to the rotor as *TSR* increases. In all cases, wake pitch increases from inner radii to the tip vortex.

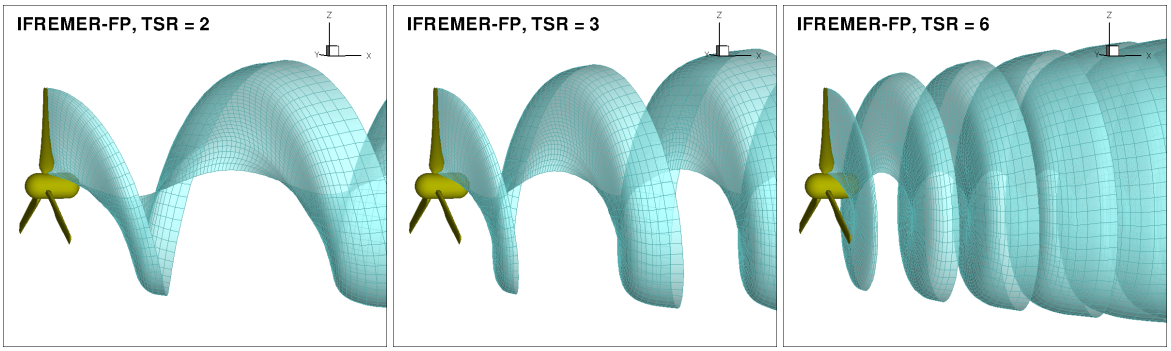

Figure 8. IFREMER-FP turbine. Trailing wake geometry of BIEM model at different operating conditions. From left to right, *TSR* = 2, 3, 6.

Viscous flow effects on blade loads are determined by applying the VFC model described in Section 2.2. The evaluation of correction factors in Eqs. (11) requires that blade section lift and drag properties are known. To this purpose, the inviscid-flow BIEM solution is used to estimate the local Reynolds number Re_r from Eq. (6), and the effective angle of attack α_e in Fig. 3, at all blade sections for the *TSR* range from zero to 8 considered in model tests. Results in left Fig. 9 show that the local Reynolds number varies between $1 \cdot 10^5$ and $3.5 \cdot 10^5$ over most of the *TSR* range of interest. Right Fig. 9 depicts a positive effective angle of attack α_e that increases from values close to zero at the highest *TSR* to 20-25 degrees for *TSR* between 1 and 2. At given *TSR* , both Reynolds and angle of attack present limited variations over a wide blade portion between 30% and 90% of span.

Experimental data of lift and drag curves of NACA 63-4xx profiles are available in the literature only at Reynolds number of 10^6 and higher, which is outside the range of interest in the present analysis as shown above. Lack of experimental data is overcome here by using numerical predictions of polar

Preprints (www.preprints.org) | NOT PEER-REVIEWED | Posted: 4 April 2018 doi:10.20944/preprints201804.0048.v1

Peer-reviewed version available at J. Mar. Sci. Eng. 2018, 6, 53; doi:10.3390/jmse6020053

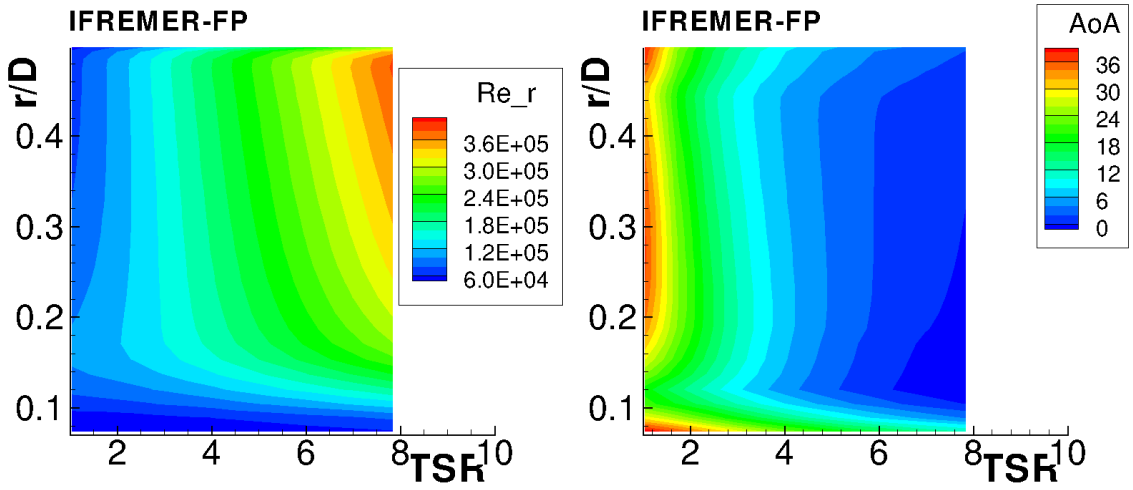

Figure 9. IFREMER-FP turbine. Reynolds number Re_r (left) and effective angle of attack α_e (right) as a function of radius r and of TSR .

curves by the X-Foil code [21]. This solver integrates a BIEM for two-dimensional, steady flow with the solution of boundary layer equations in integral form and is largely used in combination with blade element (momentum) methods. The NACA 63-421 profile corresponding to 21% thick blade sections at 70% of span is taken as representative of all blade sections. At angle of attack beyond stall, X-Foil predictions are not reliable and polar curves are completed by the following extrapolation procedure. At very high incidence angles (here, $\alpha \geq 30°$), lift and drag values are taken from experimental data for the NACA 0015 profile by Sheldahl & Klimas [22]. The assumption is that for very high angles, hydrodynamic loads are not sensitive to profile shape details. A polynomial fit is used to merge NACA 63-421 data from X-Foil and high angle of attack NACA 0015 data at angle of attack between stall and 30 degrees. This procedure to complete lift and drag information over the full angle of attack range of interest is alternative to the approach in [23] largely used in the literature.

Lift and drag curves calculated by X-Foil are presented in Fig. 10. In particular, results for 5 values of Reynolds number are considered in order to adequately describe lift and drag properties over the Re_r range of interest (left Fig. 9). Lift and drag curves from experimental data at Re =3E6 in [24] are also given for comparison.

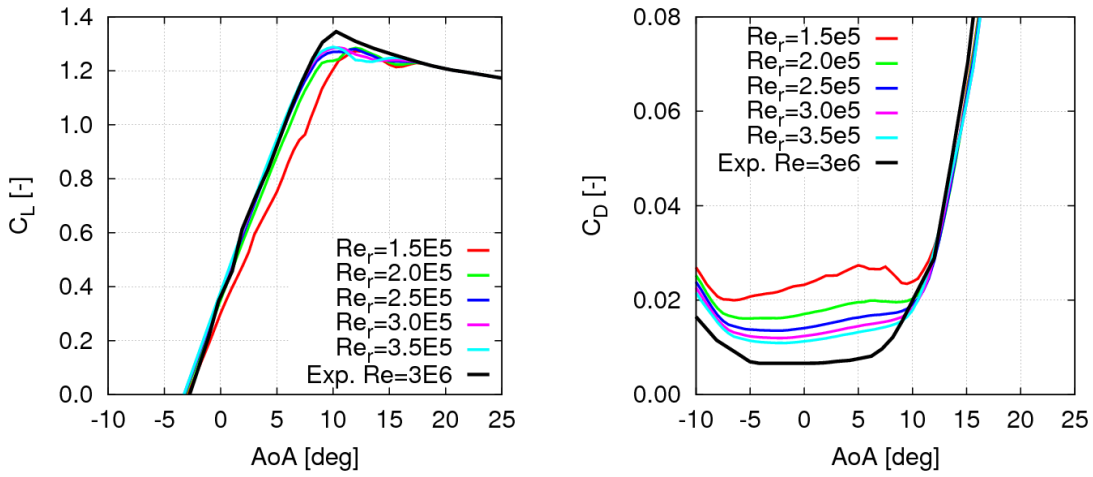

Figure 10. NACA 63-421 2D foil: lift (left) and drag (right) coefficients calculated by X-Foil and from experiments [24].

Preprints (www.preprints.org) | NOT PEER-REVIEWED | Posted: 4 April 2018 doi:10.20944/preprints201804.0048.v1

Peer-reviewed version available at J. Mar. Sci. Eng. 2018, 6, 53; doi:10.3390/jmse6020053

Figure 11 maps correction factors $\mathcal{K}_D, \mathcal{K}_L$ along blade span and over the *TSR* range of interest. Values close to one denote conditions where blade flow is attached or weakly separated and no correction of sectional loads by BIEM is needed. This occurs at $TSR \simeq 2.5$ and higher, which corresponds to effective angle of attack below 10-12 degrees, as shown in Fig. 9. At lower *TSR* , the effective angle of attack increases up to stall, as apparent from polar curves in Fig. 10. As expected, the lift factor $\mathcal{K}_L$ drops below 1, while the drag factor $\mathcal{K}_D$ rapidly grows, to simulate, respectively, stall-induced lift loss and drag rise.

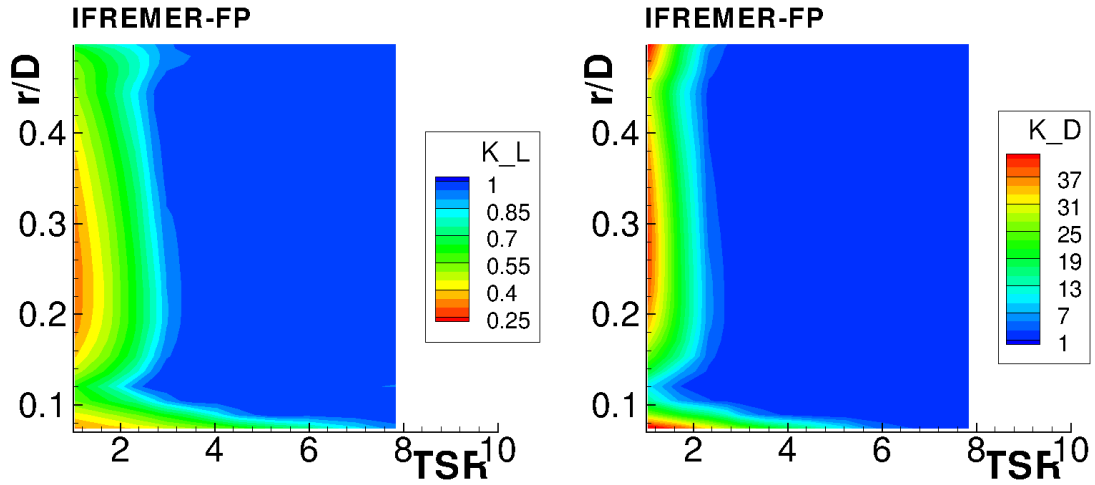

Figure 11. IFREMER-FP turbine. Correction factors for radial contributions to lift (left) and drag (right) as a function of radius r and of *TSR* .

Predicted turbine thrust, torque and power curves are presented in Fig. 12 and compared with experimental data at $V = 1.2$ m/s from three facilities involved in the round-robin test: CNR-INSEAN towing tank (INSEAN), IFREMER flume tank (IFREMER) and Kelvin Hydrodynamics Laboratory at University of Strathclyde (KHL). Results from the fourth facility participating to the round robin test, CNR-INSEAN flume tank, are omitted here since they fall within the range given by those considered in plots. For the sake of precision, measured thrust and power coefficients only are presented in [11]. Here, also the torque coefficient is considered because this quantity provides a direct indication of the accuracy of blade tangential forces evaluated by the numerical model.

It is important to observe that present experimental and numerical results use different definitions of thrust and torque. Numerical thrust and torque are determined by integrating hydrodynamic loads on blade surfaces, while in the experimental set-up, turbine torque denotes the axial moment measured by a torque sensor placed between the rotating hub and the fixed nacelle. Assuming the contribution to torque of the rotating hub is negligible, numerical and experimental data are consistent. Both numerical and experimental power are evaluated from the hydrodynamic torque Q as $P = 2\pi n Q$.

Less direct is the comparison between numerical and measured thrust. Turbine thrust reported in [11] denotes the axial force at the top of the mast supporting the turbine. This quantity combines blades thrust with a non negligible resistance contribution D_{HDM} from hub, nacelle and the mast piercing the free surface. Tests performed at IFREMER of a dummy IFREMER-FP rotor with no blades determined $D_{HDM} = 16.89N$ at $V = 0.8$ m/s (not reported in [11]). For the sake of completeness, top left Fig. 12 also presents measured axial force with the D_{HDM} contribution subtracted. This result is referred to as 'Exp IFREMER Corr.'.

Numerical results in Fig. 12 include both BIEM without viscosity correction and corrected values by Eqs. (11) (label BIEM-VFC). As expected from the discussion above, viscosity effects are negligible at *TSR* = 5 and higher, while small differences between standard BIEM (that is, with non viscous-flow

Preprints (www.preprints.org) | NOT PEER-REVIEWED | Posted: 4 April 2018 doi:10.20944/preprints201804.0048.v1

Peer-reviewed version available at J. Mar. Sci. Eng. 2018, 6, 53; doi:10.3390/jmse6020053

corrections) and BIEM-VFC predictions are noted for $3 < TSR < 5$. In this range, numerical and experimental results for torque and power are in good agreement, while thrust is underestimated in numerical results. The reason for this difference in thrust is not clear and could be related to hub, nacelle and mast resistance contributions that are only approximately subtracted from axial force measurements.

At *TSR* lower than 3, massive flow separation and stall determine a dramatic reduction of thrust, torque and power that is missed in standard BIEM results, while BIEM-VFC results capture the correct trend. In particular, measured peak values of C_Q and C_P are matched at the correct *TSR* values. At very low *TSR* , where deep stall conditions occur on blades, the BIEM-VFC model overpredicts both torque and power, but the viscous-flow correction allows to recover most of the error affecting inviscid-flow predictions by non-corrected BIEM.

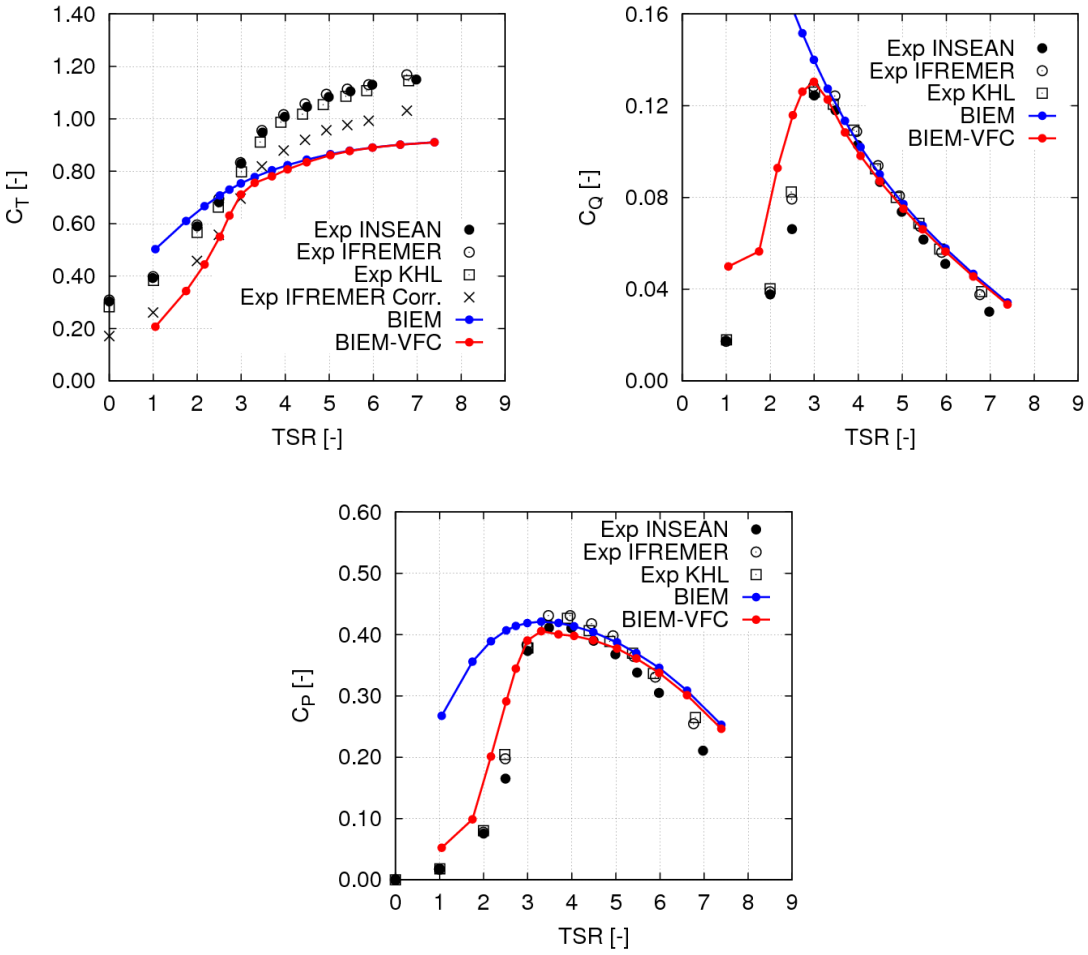

Figure 12. IFREMER-FP turbine performance predictions by BIEM and BIEM-VFC compared to experimental data in [11]: thrust (top left), torque (top right) and power (bottom) coefficients.

Figures 13 and 14 address blade pressure distributions evaluated by BIEM. Specifically, the pressure coefficient is defined as

$$C_p = \frac{p - p_0}{\frac{1}{2}\rho V_I^2}, \tag{12}$$

where the pressure p is evaluated by BIEM and $V_I(r) = [V^2 + (\Omega r)^2]^{1/2}$ is the velocity of the flow incoming to the blade section at radius r. Recalling that the VFC model applies only to global loads and not to the pressure distribution, calculated C_p is representative only in the *TSR* range where viscosity

Preprints (www.preprints.org) | NOT PEER-REVIEWED | Posted: 4 April 2018 doi:10.20944/preprints201804.0048.v1

Peer-reviewed version available at J. Mar. Sci. Eng. 2018, 6, 53; doi:10.3390/jmse6020053

correction is not significant. For the present case, this approximately holds for $TSR > 3$. Figure 13 depicts pressure distributions on blades pressure and suction sides at $TSR = 3.3$ (peak power condition, see Fig. 12). The effect of TSR on blade pressure distribution is illustrated in Fig. 14, where C_p along the blade section at $r/R = 0.7$ for three values of TSR is plotted. As expected, the pressure jump between pressure and suction sides tends to reduce as TSR is increased from the peak power condition.

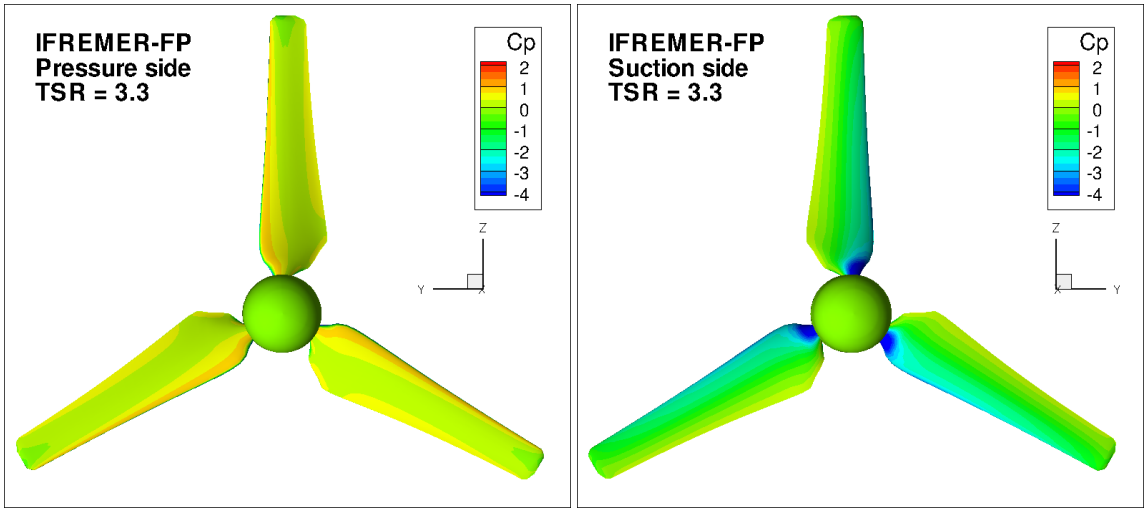

Figure 13. IFREMER-FP turbine. Pressure distribution evaluated by inviscid-flow BIEM, $TSR = 3.3$ (peak power condition).

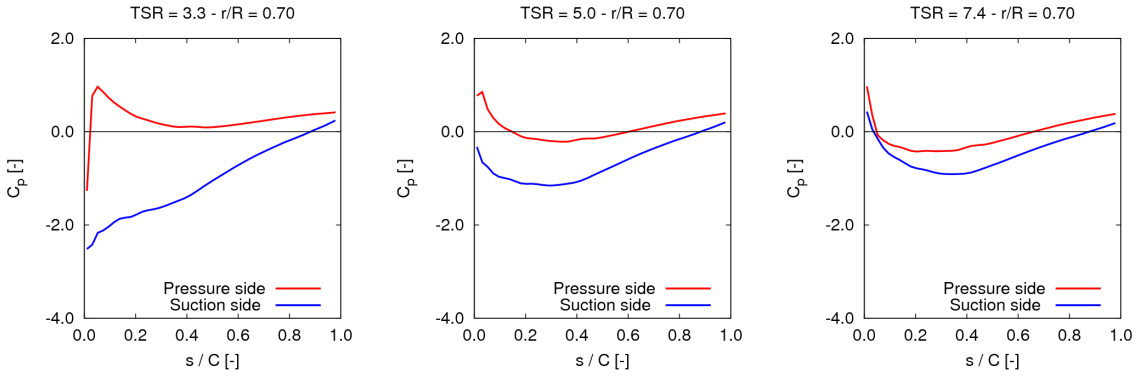

Figure 14. IFREMER-FP turbine. Pressure distribution evaluated by inviscid-flow BIEM at radial section at 70% of blade span. From left to right: $TSR = 3.3, 5, 7.4$.

5. Variable pitch turbine study

The variable-pitch UoS-VP turbine described in Bahaj et al. [13] represents a valuable benchmark to investigate the capability of a computational model to capture the effect of blade pitch variations on turbine loads and in particular to correctly describe performance in off-design conditions. As for the fixed-pitch IFREMER-FP turbine discussed above, a simplified three-dimensional model is used in which the aft portion of the nacelle and the supporting stanchion are omitted. Another difference exists at blade root where NACA 63-8xx sections are used in the computational model, while the physical model presents cylindrical sections to make possible pitch variations. Figure 15 shows the computational grid built for BIEM calculations. Discretization parameters are similar to the IFREMER-FP case.

Preprints (www.preprints.org) | NOT PEER-REVIEWED | Posted: 4 April 2018 doi:10.20944/preprints201804.0048.v1

Peer-reviewed version available at J. Mar. Sci. Eng. 2018, 6, 53; doi:10.3390/jmse6020053

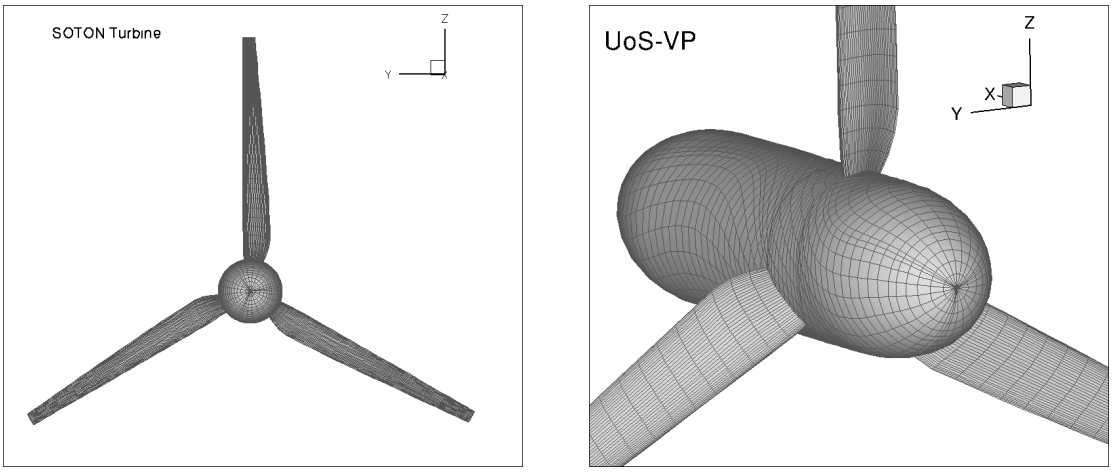

Figure 15. UoS-VP turbine. Three-dimensional model and details of the computational grid for BIEM analysis.

Figure 16 depicts the intensity of wake-induced velocity $v_{x,w}$ from Eq. (7) evaluated by BIEM at axial locations corresponding to rotor blade trailing edge and 70% of blade span. Different blade pitch settings and a range of operating conditions corresponding to model tests are plotted. The resulting trailing wake surfaces for the design condition $\Phi = 20^\circ$ and for three representative values of *TSR* are shown in Fig. 17.

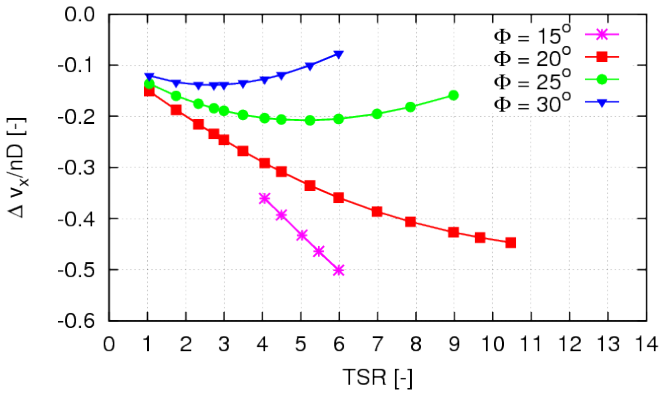

Figure 16. UoS-VP turbine. Axial induced velocity distribution at rotor plane and 70% of blade span. Different pitch settings Φ compared.

Turbine operating conditions considered in the present analysis refer to selected cavitation tunnel test conditions from [13] as summarized in Table 3.

Recalling Eq. (6), Reynolds number Re_r characterizing blade section flow at radius r depends on the inflow velocity V. Figure 18 maps its distribution as a function of radius and *TSR* for pitch setting $\Phi = 20^\circ$, while Fig. 19 compares Re_r at 70% of blade chord for the highest and lowest inflow speed cases from Table 3. Results indicate that Re_r approximately varies between $1 \cdot 10^5$ and $3.5 \cdot 10^5$ over most of the operating range of interest here.

Table 3. UoS-VP turbine. Inflow speed conditions.

Blade pitch setting, Φ [deg]	15	20	25	27	30
Inflow speed, V [m/s]	1.40	1.73	1.54	1.30	1.54

Preprints (www.preprints.org) | NOT PEER-REVIEWED | Posted: 4 April 2018 doi:10.20944/preprints201804.0048.v1

Peer-reviewed version available at J. Mar. Sci. Eng. 2018, 6, 53; doi:10.3390/jmse6020053

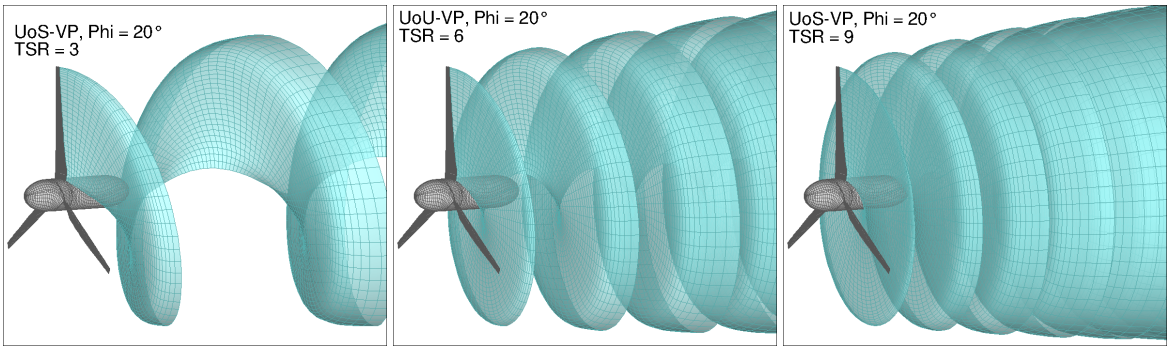

Figure 17. UoS-VP turbine. Wake geometry of BIEM model at different operating conditions. From left to right, $TSR = 3, 6, 9$. Design pitch setting, $\Phi = 20°$.

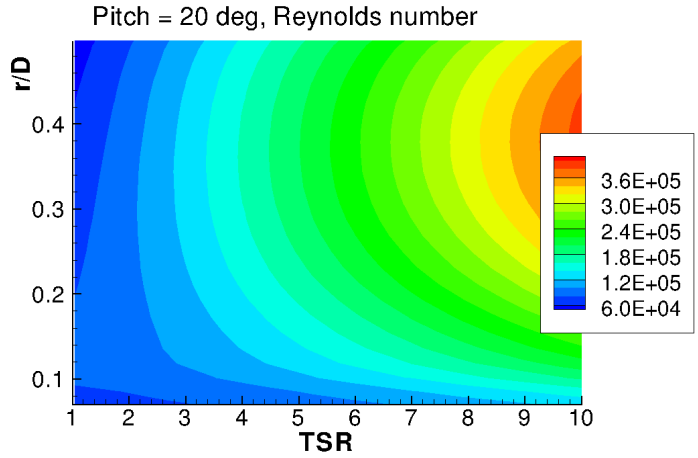

Figure 18. UoS-VP turbine. Reynolds number Re_r as a function of radius r and of turbine operating condition (TSR).

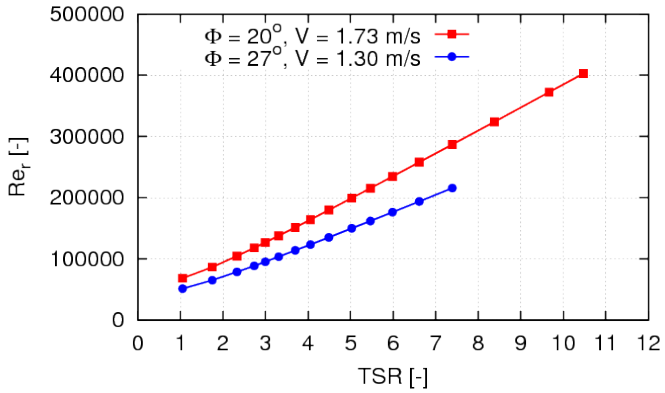

Figure 19. UoS-VP turbine. Reynolds number Re_r at radius $r/R = 0.7$ for pitch settings corresponding to the highest inflow speed ($V = 1.73$ m/s, $\Phi = 20°$), and for the lowest inflow speed ($V = 1.3$ m/s, $\Phi = 27°$).

375 The effective angle of attack α_e evaluated by standard BIEM is presented in Fig. 20. Specifically, α_e
376 distributions along blade span at variable TSR are presented for design pitch setting, $\Phi = 20°$, and

Preprints (www.preprints.org) | NOT PEER-REVIEWED | Posted: 4 April 2018 doi:10.20944/preprints201804.0048.v1

Peer-reviewed version available at J. Mar. Sci. Eng. 2018, 6, 53; doi:10.3390/jmse6020053

Fig. 21 presents the variability of this quantity at different pitch settings at 70% of blade span. Case $\Phi = 20^\circ$ shows blade sections mostly operating in the range $-5^\circ < \alpha_e < 25^\circ$ with higher values only at $TSR < 2$. As expected, larger pitch angles determine lower α_e values.

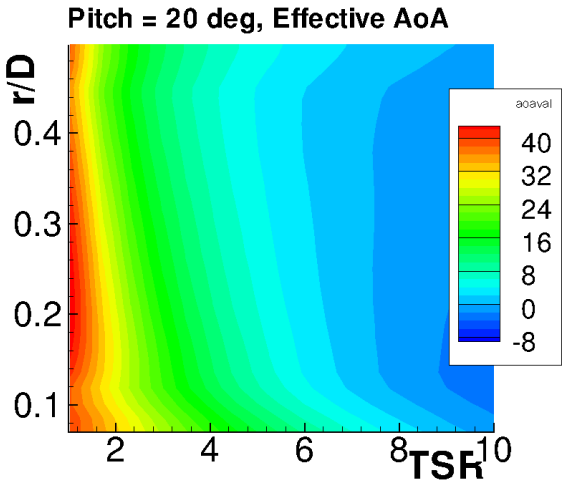

Figure 20. UoS-VP turbine. Effective angle of attack α_e as a function of radius r and of turbine operating condition (TSR). Design pitch setting $\Phi = 20^\circ$.

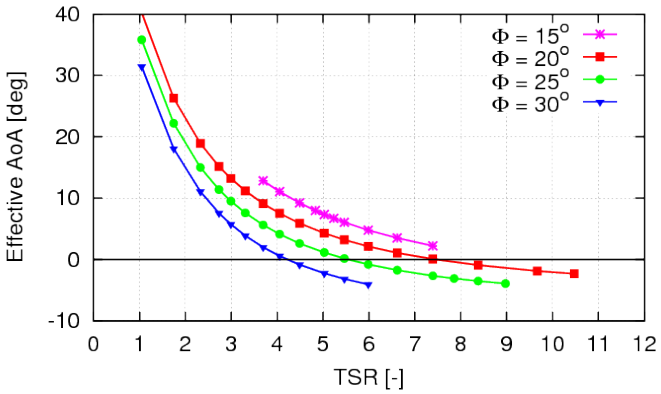

Figure 21. UoS-VP turbine. Effective angle of attack α_e at radius $r/R = 0.7$ for different pitch settings and TSR.

Reference [25] provides lift and drag curves of the NACA 63-815 foil at $Re = 8 \cdot 10^5$. This 15% thick foil is taken as representative of UoS-VP turbine sections whose thickness ratio varies from 0.176 at 50% of span to 0.126 at tip. Recalling Fig. 19, $Re = 8 \cdot 10^5$ is quite higher than the range of interest in the present analysis. In order to obtain lift and drag data in the actual Re_r and α_e ranges, the X-Foil code is used and 6 polar curves for $1.5 < Re_r < 4.0 \cdot 10^5$ are evaluated. Polar data are completed at very high angle of attack using NACA 0015 profile data and polynomial interpolation as described in Section 3.2 for the IFREMER-FP turbine. Resulting lift and drag curves are plotted in Fig. 22 and experimental data from [25] are also shown for comparison. Lift curves show that stall conditions are predicted by X-Foil at about 10-12 degrees, while experimental data show a more gradual transition to stall between 8 and 12 degrees. Results for drag are in agreement only at negative angle of attack, while experimental data present quite larger C_D values than X-Foil between 2 and 12 degrees. These differences cannot be explained because of the different Re numbers in the two datasets. Furthermore, drag measurements also denote a large scattering.

Preprints (www.preprints.org) | NOT PEER-REVIEWED | Posted: 4 April 2018 doi:10.20944/preprints201804.0048.v1

Peer-reviewed version available at J. Mar. Sci. Eng. 2018, 6, 53; doi:10.3390/jmse6020053

Lift and drag properties predicted by X-Foil are used to feed the viscous-flow correction model described in Section 2. Contour maps in Fig. 23 show $\mathcal{K}_L$ and $\mathcal{K}_D$ factors for design pitch setting $\Phi = 20°$, while Fig. 24 depicts the variation of these quantities at $r/R = 0.7$ over the pitch settings range. In case $\Phi = 20°$, viscosity effects on blade section lift and drag are negligible at *TSR* of about 3.5-4 and higher, which corresponds to non-separated flow conditions at angle of attack below 8-10 degrees, see Fig. 20 and Fig. 22. At lower *TSR* , the lift correction factor $\mathcal{K}_L$ gradually decreases to about 0.3 (lift loss under stall) while the drag correction factor $\mathcal{K}_D$ suddenly increases to values of 30 and more (drag crisis).

Consistent with sectional angle of attack values commented above, pitch settings $\Phi > 20°$ limit flow separation and stall effects to very low values of *TSR* , while in case $\Phi = 15°$, most of the addressed operating range is under the effect of flow separation and stall.

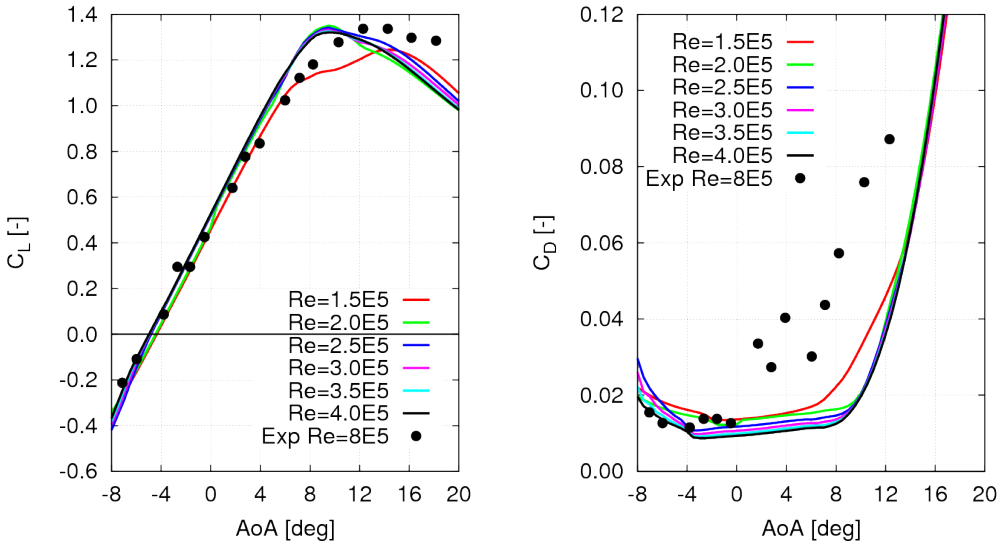

Figure 22. NACA 63-815 2D foil: lift (left) and drag (right) coefficients used for the viscous-flow correction of BIEM.

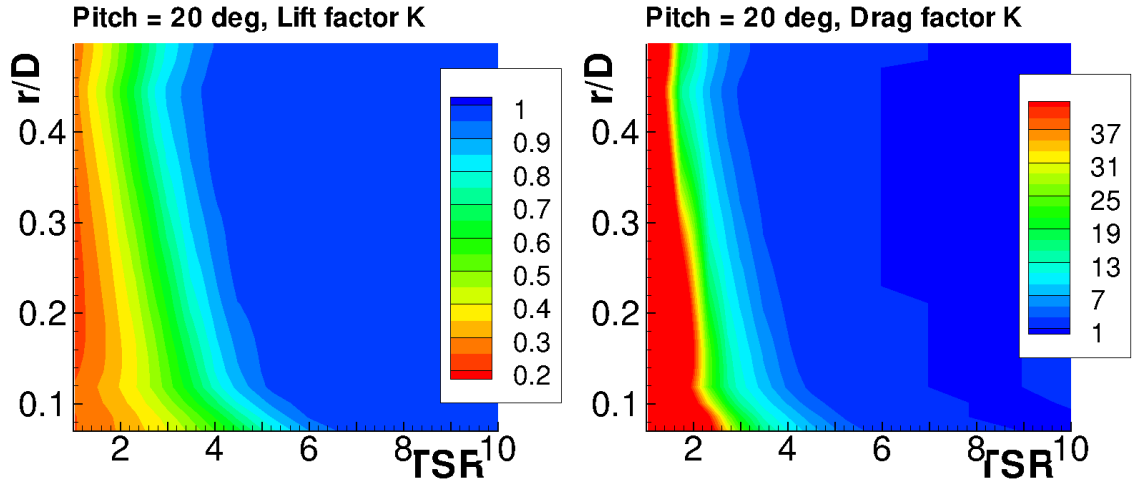

Figure 23. UoS-VP turbine. Correction factors for radial contributions to lift (left) and drag (right) as a function of radius *r* and of operating condition (*TSR*). Pitch setting $\Phi = 20°$.

Turbine thrust and power predictions by BIEM and by BIEM-VFC using blade section polar data from X-Foil are compared with model test measurements from [13] in Figs. 25 and 26. In general, it

Preprints (www.preprints.org) | NOT PEER-REVIEWED | Posted: 4 April 2018 doi:10.20944/preprints201804.0048.v1

Peer-reviewed version available at J. Mar. Sci. Eng. 2018, 6, 53; doi:10.3390/jmse6020053

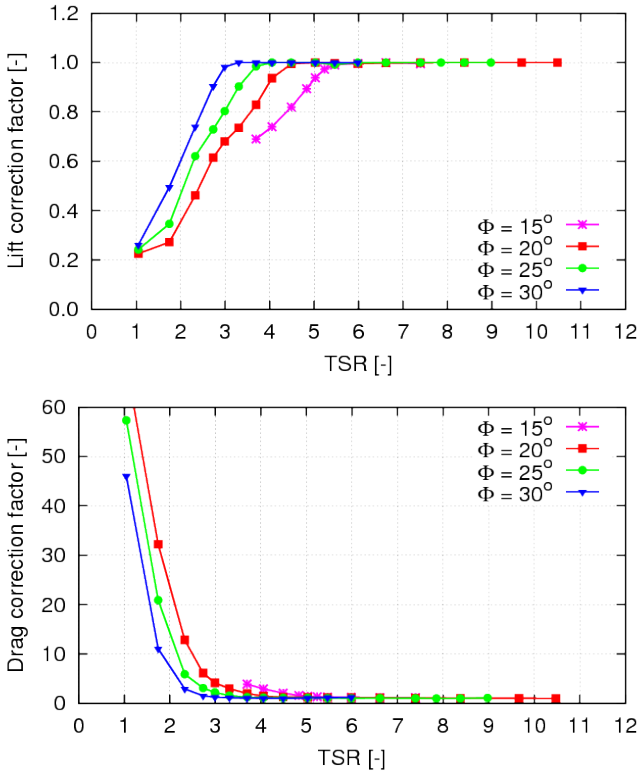

Figure 24. UoS-VP turbine. Lift correction factor $\mathcal{K}_L$ (top) and drag correction factor $\mathcal{K}_D$ (bottom) at radius $r/R = 0.7$ for different Pitch settings.

may be noted that standard BIEM predictions of both thrust and power fairly reproduce experimental data only in the high *TSR* range for pitch setting cases $20° < \Phi < 27°$. For operating conditions corresponding to peak power *TSR* and lower values of *TSR* , standard BIEM results overpredict both thrust and power, since the effects of blade flow separation and stall are not captured. When the VFC model is applied to correct BIEM, predicted thrust and power are in fair agreement with measured data over a full *TSR* range. For extreme off-design cases $\Phi = 15°$ and $\Phi = 30°$, large differences between numerical and experimental results are observed even if the viscous-fow correction is applied. In particular, at $\Phi = 15°$ predicted C_T presents an unphysical trend with increasing *TSR* . A possible explanation of this result is that under extreme off-design conditions, blade flow is affected by a complex separated flow phenomenology that is beyond the limits of the proposed VFC model, and a detailed CFD analysis would be necessary. Unfortunately, experimental data do not give information at very low *TSR* where deep-stall conditions are expected. Large scattering of measured thrust and power is also noted in extreme off-design conditions.

The capability of the BIEM-VFC model to correctly describe turbine performance trends at different pitch settings can be discussed considering results in Fig. 27, where four performance indicators are considered: maximum value of thrust coefficient $C_{T_{max}}$, maximum value of power coefficient $C_{P_{max}}$, and corresponding values of *TSR* where maxima are established. Numerical predictions by BIEM-VFC and polar data from X-Foil (label: VFC, XFOIL Polar) are compared with polynomial fits of experimental data from cavitation tunnel tests as presented in Fig. 7 of [13] (label: Model tests). Numerical results by BIEM-VFC using experimental data for blade section lift and drag taken from measurements in [25] are also presented (label: VFC, Exp. Polar).

Quantity $C_{T_{max}}$ by BIEM-VFC and X-Foil and the corresponding *TSR* values fairly reproduce the trend observed in experiments over the range $20° < \Phi < 30°$. Same comments can be made for the maximum power except for case $\Phi = 30°$, where predicted $C_{P_{max}}$ is some 20% lower than measured.

Preprints (www.preprints.org) | NOT PEER-REVIEWED | Posted: 4 April 2018 doi:10.20944/preprints201804.0048.v1

Peer-reviewed version available at J. Mar. Sci. Eng. 2018, 6, 53; doi:10.3390/jmse6020053

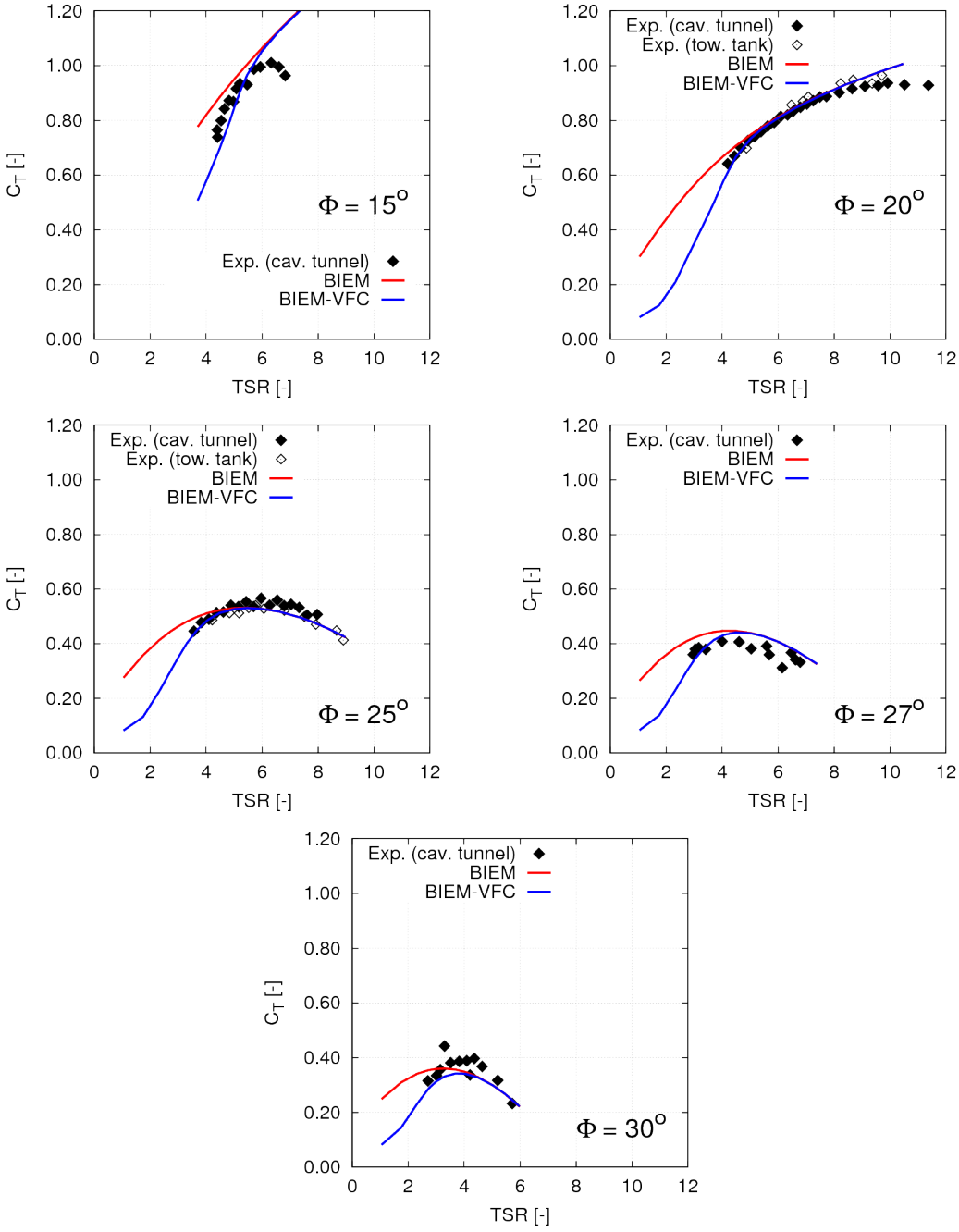

Figure 25. UoS-VP turbine performance predictions by BIEM and BIEM-VFC compared to experimental data in [13]. Thrust coefficient at pitch settings $\Phi = 15°, 20°, 25°, 27°, 30°$.

However, fitted experimental data at $\Phi = 30°$ show a rather inconsistent trend with Φ. At off-design pitch $\Phi = 15°$, BIEM-VFC and X-Foil results match experimental data for $C_{P_{max}}$ and the corresponding *TSR* , while the $C_{T_{max}}$ prediction is not plotted since numerical results show an unphysical trend with increasing *TSR* as already discussed.

Figure 27 allows to compare BIEM-VFC results based on X-Foil predictions of sectional lift and drag properties with those obtained by considering measured lift and drag in [25]. As already commented in Fig. 22, measured drag is much higher than X-Foil predictions over a significant range of angle of attack. As expected, this turns into underestimated turbine power coefficient, bottom left

Preprints (www.preprints.org) | NOT PEER-REVIEWED | Posted: 4 April 2018 doi:10.20944/preprints201804.0048.v1

Peer-reviewed version available at J. Mar. Sci. Eng. 2018, 6, 53; doi:10.3390/jmse6020053

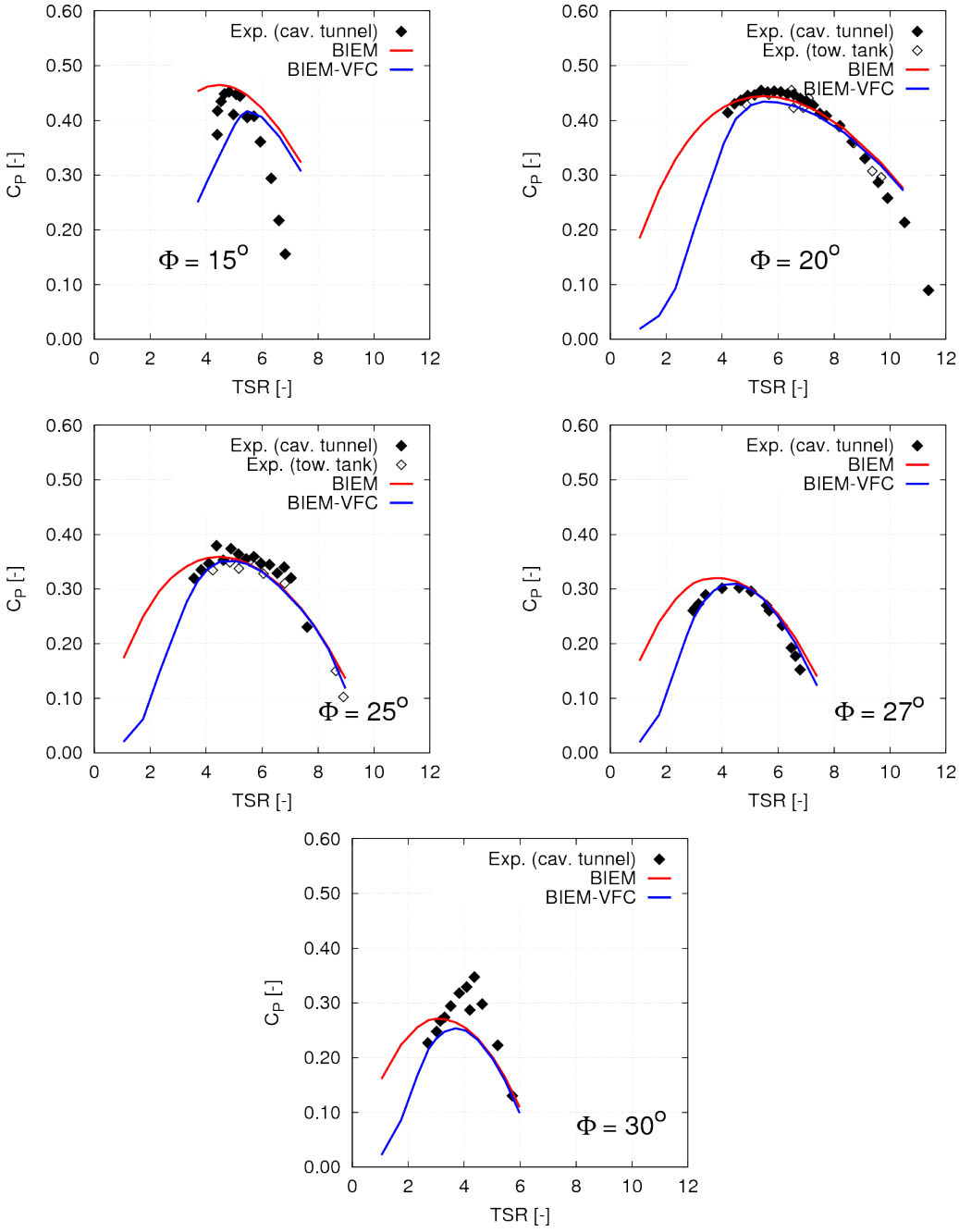

Figure 26. UoS-VP turbine performance predictions by BIEM and BIEM-VFC compared to experimental data in [13]. Power coefficient at pitch settings $\Phi = 15°, 20°, 25°, 27°, 30°$.

Fig. 27. Smaller differences between measured and X-Foil lift observed in left Fig. 22, have a negligible effect on predicted turbine thrust coefficient, as shown in top Fig. 27.

In order to complete the present validation study, it is also interesting to compare results by the proposed BIEM-VFC approach with data from the literature obtained using different computational models. Two cases are considered here: Bahaj et al. [26] present results by two solvers based on Blade Element Method (BEM) for pitch settings from $\Phi = 15°$ to $27°$. Next, Baltazar & Falcão de Campos [6] present results by BIEM with viscous flow corrections for cases $\Phi = 20°$ and $25°$.

Preprints (www.preprints.org) | NOT PEER-REVIEWED | Posted: 4 April 2018 doi:10.20944/preprints201804.0048.v1

Peer-reviewed version available at J. Mar. Sci. Eng. 2018, 6, 53; doi:10.3390/jmse6020053

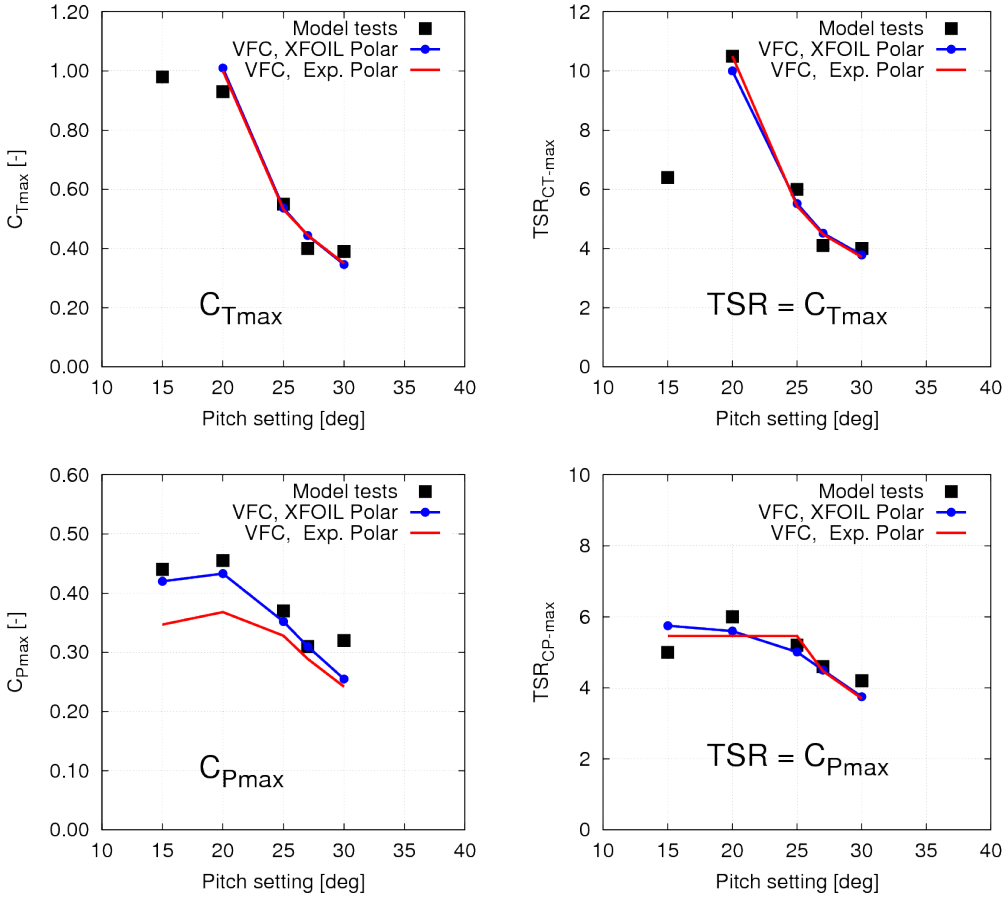

Figure 27. UoS-VP turbine. Effect of pitch setting Φ: from top to bottom, left to right, $C_{T_{max}}$, $C_{P_{max}}$ and corresponding *TSR* values.

Thrust coefficient predictions are compared in Fig. 28. Results by BEM solvers GH-Tidal and SERG-Tidal show an accuracy with respect to model test results in [13] that is broadly comparable to what is obtained using the present BIEM-VFC. Predictions by BIEM-VFC and GH-Tidal are closer to experiments than SERG-Tidal for pitch settings $\Phi = 20°, 25°, 27°$, while the opposite holds for $\Phi = 27°$. This trend is only in part confirmed in Fig. 29 where power coefficient results are shown.

While BIEM-VFC and SERG-Tidal show a comparable accuracy for C_P at $\Phi = 20°, 25°, 27°$, results by GH-Tidal overestimate experimental data. It is also noted that off-design case $\Phi = 15°$ shows similar results between BEM and the present BIEM-VFC for the thrust coefficient, while power coefficient results are very different, with BEM models fairly capturing power peak and failing to predict results at higher *TSR*. Finally, thrust and power by the BIEM model with viscous correction presented in Baltazar & Falcão de Campos [6] are underestimated for both pitch setting cases addressed. It is interesting to observe that results comparable to present BIEM-VFC model are obtained in [6] by considering only drag correction of standard BIEM predictions. Details of this further comparison are not given here for the sake of conciseness.

6. Discussion

The analysis of present results compared to reference data from the literature highlights the importance of adding a viscous-flow correction to standard BIEM results obtained under inviscid-flow assumptions. Although simple and partially based on semi-empirical corrections, the proposed BIEM-VFC approach allows to significantly improve the reliability of turbine performance predictions by BIEM over a full range of operating conditions, including design and off-design blade pitch settings.

Preprints (www.preprints.org) | NOT PEER-REVIEWED | Posted: 4 April 2018 doi:10.20944/preprints201804.0048.v1

Peer-reviewed version available at J. Mar. Sci. Eng. 2018, 6, 53; doi:10.3390/jmse6020053

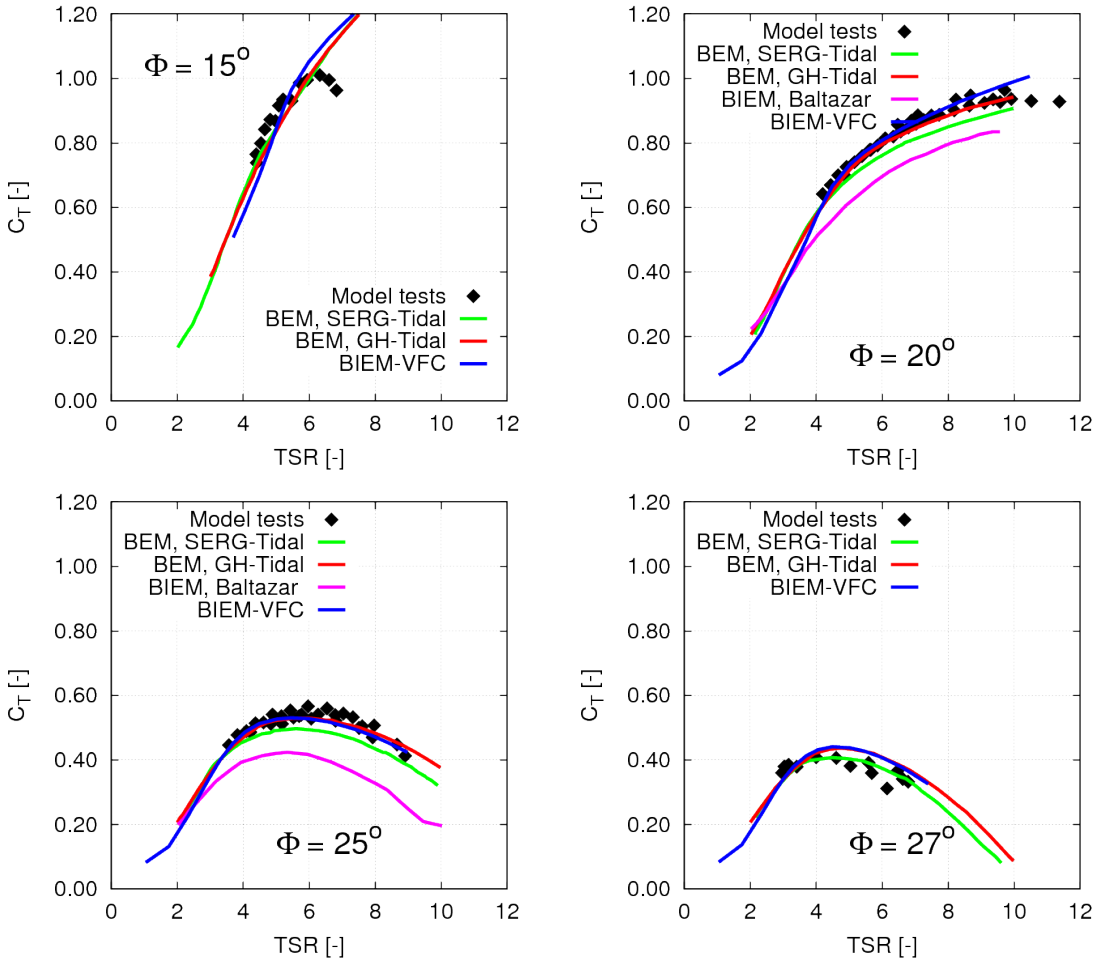

Figure 28. UoS-VP turbine performance predictions by BIEM-VFC compared to results from the literature: thrust coefficient C_T. Pitch settings $\Phi = 15°$ to $27°$.

Main advantage of BIEM modelling with respect to blade element momentum methods routinely used for marine turbines is the possibility to determine a consistent representation of the three-dimensional flow around rotor blades and hub in steady or unsteady flow. Pressure distributions on the blade surface can be used as input to predict the occurrence of cavitation and to estimate its detrimental effects in terms of vibrations, noise, erosion.

Nonetheless, a major weakness of the present BIEM-VFC approach is that viscosity correction applies only to blade loads and not to the potential flow solution as a whole. In particular, the correction does not apply to the intensity of the vortex sheet shed at blade trailing edge, nor to the induced velocity field necessary to evaluate the effective angle of attack. Neglecting these effects is expected to be the source of errors in performance predictions when the turbine operates at *TSR* lower than the peak power condition.

To overcome this limitation, a generalization of the present VFC model is the subject of work underway. Specifically, trailing vorticity distributions that are compatible with the correction of blade loads determined by the VFC scheme described in Section 2.2 can be obtained through an iterative procedure in which the direct relationship between axial and tangential force contributions by a blade element at radius r and turbine-induced velocity perturbation is derived by momentum and moment of momentum balance. Furthermore, the boundary integral representation (2) is generalised to include additional source terms according to the viscous/inviscid coupling methodology proposed in [27].

Preprints (www.preprints.org) | NOT PEER-REVIEWED | Posted: 4 April 2018 doi:10.20944/preprints201804.0048.v1

Peer-reviewed version available at J. Mar. Sci. Eng. 2018, 6, 53; doi:10.3390/jmse6020053

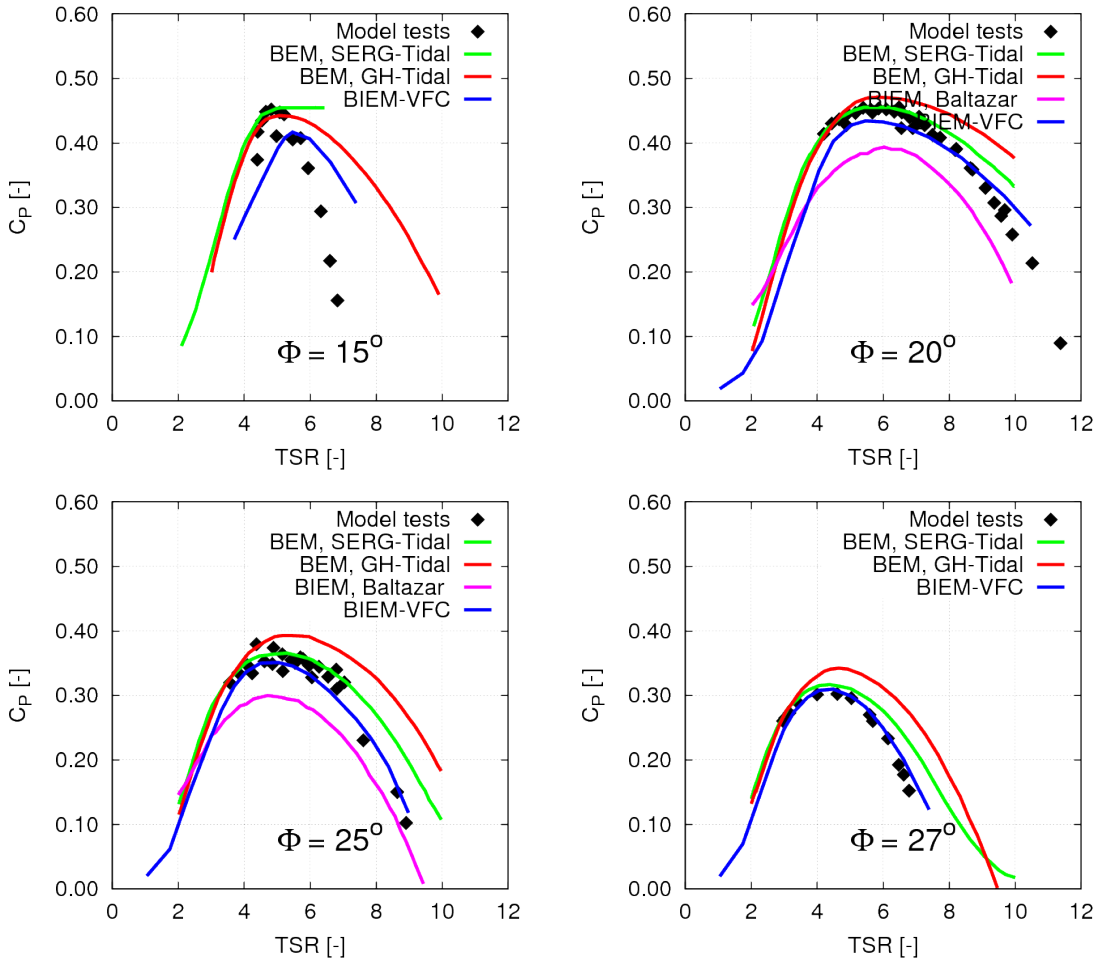

Figure 29. UoS-VP turbine performance predictions by BIEM-VFC compared to results from the literature: power coefficient C_p. Pitch settings $\Phi = 15°$ to 27°.

In addition to single turbine performance studies, the BIEM-VFC methodology is also applied to study the hydrodynamic behaviour of turbines operating in arrays. In this case, the inviscid-flow BIEM with VFC model is combined with a viscous flow solver (Reynolds-Averaged Navier-Stokes, RANS) to correctly describe the turbulent, vortical stream that characterizes the inflow to a turbine in the wake of similar devices placed upstream. An application of this combined BIEM-VFC and RANS computational methodology has been discussed by the authors in [28] where a preliminary study by BIEM-VFC of the IFREMER-FP test case addressed above is also addressed.

7. Conclusions

A computational methodology for the hydrodynamic analysis of horizontal-axis marine current turbines has been presented, and results of a validation study have been discussed. The approach is based on a Boundary Integral Equation Model (BIEM) for inviscid flows that is combined with a trailing wake model specific for hydrokinetic turbines and with a viscous flow correction model (VFC) to include blade flow separation and stall effects on predicted hydrodynamic loads. The latter is derived by a semi-empirical approach in which inviscid-flow blade loads by BIEM are corrected on the basis of lift and drag properties of two-dimensional foils describing blade sections under equivalent three-dimensional flow conditions.

Numerical predictions by BIEM-VFC have been validated through comparisons with experimental data and with numerical results from the literature. The analysis highlights the capability of the

proposed methodology to correctly describe turbine performance over a full range of operating conditions. Specifically, reliable predictions of turbine thrust, torque and power are obtained at medium/high Tip Speed Ratio (TSR) regimes, when blade flow is mostly attached, but also at relatively low TSR , where blade flow separation and stall determine thrust loss and drag crisis. More in details, good predictions of turbine performance are obtained for blade pitch settings close to design, while discrepancies for both thrust and torque (power) are observed in off-design conditions.

Comparing BIEM-VFC with other computational models in the literature, a key finding is that the accuracy the proposed approach is aligned with blade element methods that are routinely used for the analysis and design of marine as well as wind turbines. Such a result is particularly important in that the present methodology based on BIEM provides a physically consistent description of the three-dimensional flow around a turbine in arbitrary onset flow, while blade element methods rely on taylored, case-dependent corrections for blade tip effects, for blade/hub interaction, number of blades. Well known limitations of blade element methods to analyse non-uniform flow conditions as well as to study turbine cavitation are also overcome through the more general description of turbine flow obtained by a BIEM approach.

Future work will address the generalization of the present VFC scheme to achieve trailing vorticity distributions and induced velocity distributions that are fully consistent with the viscosity correction applied on blade loads. Further validation studies will focus the capability of the generalised BIEM-VFC model to predict turbine performance at low TSR and when turbine blades operate in off-design conditions.

Acknowledgments: The work described has been funded under the CNR-INSEAN Project ULYSSES (Underpinning LaboratorY for Studies on Sea Energy Systems). The authors wish to thank Dr. Benoit Gaurier for his kind support in the analysis of validation data from experiments at IFREMER. Part of validation data have been developed under the EU-FP7 MaRINET Project (Grant 262552).

Author Contributions: Francesco Salvatore and Zohreh Sarichloo developed the original viscous-flow correction and trailing wake models while Danilo Calcagni and Francesco Salvatore adapted the existing BIEM model. Zohreh Sarichloo and Francesco Salvatore were responsible for computational model validation studies. All the authors contributed to results analysis and discussion.

Conflicts of Interest: The authors declare no conflict of interest.

Appendix Nomenclature

Symbol	Description	Units
c	Turbine blade chord	[m]
C_p	Pressure coefficient	[-]
C_P	Power coefficient	[-]
C_F	Friction coefficient	[-]
C_Q	Torque coefficient	[-]
C_T	Thrust coefficient	[-]
D	Turbine diameter, $2R$	[m]
D	Drag	[N]
J	Advance coefficient, V/nD	[-]
$\mathcal{K}_D$	Drag correction factor	[-]
$\mathcal{K}_L$	Lift correction factor	[-]
L	Lift	[N]
n	Turbine rotational speed	[s^{-1}]
P	Turbine power	[W]
p_0	Reference pressure	[Pa]
Q	Turbine torque	[Nm]
R	Turbine radius	[m]
Re_r	Reynolds number, Eq. (6)	[-]
T	Turbine thrust	[N]
TSR ; λ	Tip Speed Ratio	[-]
V	Freestream velocity	[ms^{-1}]
α	angle of attack	[deg]
ν	Kynematic viscosity	[m^2s^{-1}]
ϕ	Velocity scalar potential	[m^2s^{-1}]
Ω	Turbine rotational speed	[$rads^{-1}$]
ϕ	Wake (linear) pitch	[m]
Φ	Blade pitch	[deg]
ρ	Water density	[kgm^{-3}]

References

1. Hansen, M. O. L. *Aerodynamics of Wind Turbines.*, 2nd Ed.; Earthscan: London, U.K., 2008.
2. Buhl, M.L.Jr. A New Empirical Relationship between Thrust Coefficient and Induction Factor for the Turbulent Windmill State. *Technical Report NREL/TP-500-36834*, **2005**.
3. Shen, W. Z., Mikkelsen, R., Sœrensen, J. N., Bak, C. Tip Loss Corrections for Wind Turbine Computations. *Wind Energy*, **2005**, *8*, 457-475.
4. Young, Y.L., Motley, M.R., Yeung, R.W. Three-Dimensional Numerical Modeling of the Transient Fluid-Structural Interaction Response of Tidal Turbines. *Journal of Offshore Mechanics and Arctic Engineering*, **2010**, *132*, 1-12.
5. He, L., Xu, W., and Kinnas, S.A. Numerical Methods for the Prediction of Unsteady Performance of Marine Propellers and Turbines., In Proceedings of the *ISOPE 2011* Twenty-first International Offshore and Polar Engineering Conference, Maui, Hawaii, 19-24 June 2011.
6. Baltazar, J., Falcão de Campos, J.A.C. Unsteady Analysis of a Horizontal Axis Marine Current Turbine in Yawed Inflow Conditions With a Panel Method. In Proceedings of the *SMP'09* First International Symposium on Marine Propulsors, Norway, 22-24 June 2009; Koushan, K., Steen, S., Eds; MARINTEK (Norwegian Marine Technology Research Institute); Trondheim, Norway, 2009.
7. Baltazar, M.J., Falcão de Campos, J.A.C. Hydrodynamic design and analysis of horizontal axis marine current turbines with lifting line and panel methods. In Proceedings of the *OMAE2011* ASME 30th Int. Conference on Ocean, Offshore and Arctic Engineering, Rotterdam, The Netherlands, 19–24 June 2011; The American Society of Mechanical Engineers; Rotterdam, The Netherlands, 2011; *5*, 453-465.

8. Salvatore, F., Testa, C., Greco, L. A Viscous/Inviscid Coupled Formulation for Unsteady Sheet Cavitation Modelling of Marine Propellers. In Proceedings of the *CAV 2003* Fifth International Symposium on Cavitation, Osaka, Japan, 1-4 November 2003.
9. Salvatore, F. Greco, L., Calcagni, D. Computational analysis of marine propeller performance and cavitation by using an inviscid-flow BEM model. In Proceedings of the *SMP'11* Second Int. Symposium on Marine Propulsion, Hamburg, Germany, 15-17 June 2011.
10. Pereira, F., Salvatore, F., Di Felice, F. Measurement and Modelling of Propeller Cavitation in Uniform Inflow. *Journal of Fluids Engineering*, **2004**, *126*, 671-679.
11. Gaurier, B., Germain, G., Facq, J.–V., Johnstone, C. M., Grant, A. D. Day, A. H., Nixon, E., Di Felice, F., Costanzo, M. Tidal energy Round Robin tests: comparisons between towing tank and circulating tank results. *Int. Journal of Marine Energy*, **2015**, *12*, 87–109.
12. EU-FP MaRINET Project. Available online: https://cordis.europa.eu/project/rcn/98372_en.html (accessed on 29 March 2018).
13. Bahaj, A.S.; Molland, A.F.; Chaplin, J.R.; Batten, W.M.J. Power and thrust measurements of marine current turbines under various hydrodynamic flow conditions in a cavitation tunnel and a towing tank. *Renewable Energy*, **(**2007), *32*, 407–426.
14. Morino, L. 'Boundary Integral Equations in Aerodynamics.' *Applied Mechanics Reviews*, **1993**, *46(8)*, 445-466.
15. Greco, L., Salvatore, F., Di Felice, F. Validation of a Quasi–potential Flow Model for the Analysis of Marine Propellers Wake. In Proceedings of the *ONR-2004* Twenty-fifth ONR Symposium on Naval Hydrodynamics, St. John's, Newfoundland, Canada, 2004; National Academies Press: Washington, DC, USA, 2004.
16. Carlton, J.S. *Marine Propellers and Propulsion*, 1st Ed.; Butterworth–Heinemann: Oxford, UK., 1994.
17. Betz, A. The Maximum of the Theoretically Possible Exploitation of Wind by Means of a Wind Motor. *Wind Engineering*, **2013**, *37(4)*, 441-446. (Translation by Hamann et al. of original paper published in 1920 by the author in German).
18. Okulov, V.L., Sørensen, J.N. Maximum efficiency of wind turbine rotors using Joukowsky and Betz approaches. *Journal of Fluid Mechanics*, **2010**, *649*, 497-508.
19. Micek, P., Gaurier, B., Germain, G., Pinon, G., Rivoalen, E. Experimental study of the turbulence intensity effects on marine current turbines behaviour. Part I: One single turbine. *Renewable Energy*, **2014**, *66*, 729-746.
20. Del Frate, C., Di Felice, F., Alves Pereira, F., Romano, G.P., Dhomé, D., Allo, J.–C. Experimental Investigation of the turbulent flow behind a horizontal axis tidal turbine. In *Progress in renewable Energies Offshore*, Proceedings of the RENEW 2016 2nd Int. Conference on Renewable Energies Offshore, Lisbon, Portugal, 24-26 October 2016.
21. Drela, M. XFOIL: An Analysis and Design System for Low Reynolds Number Airfoils. In *Low Reynolds Number Aerodynamics.* Proceedings of the Conference Notre Dame, Indiana, USA, 5-7 June 1989; Lecture Notes in Engineering, Bd. 54; Springer Berlin: Heidelberg, 1989; 1–12; 978-3-540-51884-6.
22. Sheldahl, R.E., Klimas, P.C. Aerodynamic Characteristics of Seven Symmetrical Airfoil Sections Through 180-Deg. Angle of Attack for Use in Aerodynamic Analysis of Vertical Axis Wind Turbines. *Report SAND80-2114, SANDIA*, **1981**, Albuquerque, NM, USA.
23. Viterna, L. A., Corrigan, R. D. Fixed pitch rotor performance of large horizontal axis wind turbines. DOE/NASA workshop on large HAWTs. Cleveland, Ohio, 1981.
24. Abbott, I. R.; von Doenhoff, A. E. Summary of airfoil data. *NACA Report 824*, **1945**.
25. Molland, A.F., Bahaj, A.S., Chaplin, J.R., Batten, W.M.J. Measurements and predictions of forces, pressures and cavitation on 2D sections suitable for marine current turbines. *Journal of Engineering for the Maritime Environment*, **2004**, *218(2)*, 127-138.
26. Bahaj, A., Batten W., McCann, G. Experimental verifications of numerical predictions for the hydrodynamic performance of horizontal axis marine current turbines. *Renewable Energy*, **2007**, *32*, 2479–2490.
27. Morino, L., Salvatore, F., Gennaretti, M. A New Velocity Decomposition for Viscous Flows: Lighthill's Equivalent-Source Method Revisited. *Computer Methods in Applied Mechanics and Engineering* **1999**, **173**(3-4), 317-336.
28. Salvatore, F., Calcagni, D., Sarichloo, Z. Development of a Viscous/Inviscid Hydrodynamics Model for Single Turbines and Arrays. In Proceedings of the *EWTEC 2017* Twelfth European Wave and Tidal Energy Conference, Cork, Ireland, 27 August - 1 September 2017.